

1 **A dataset on the structural diversity of European forests**

2

3 Marco Girardello*^{1,2}, Gonzalo Oton*¹, Matteo Piccardo³ Mark Pickering³, Agata Elia³, Guido
4 Ceccherini¹, Mariano Garcia⁴ Mirco Migliavacca¹ Alessandro Cescatti¹

5 ¹European Commission, Joint Research Centre, Italy

6 ²Discipline of Geography, School of Natural Sciences, Trinity College Dublin, Dublin, Ireland

7 ³Consultant of European Commission, Joint Research Centre, Italy

8 ⁴Universidad de Alcalá, Department of Geology, Geography and the Environment, Environmental Remote Sensing Research
9 Group, C/ Colegios, 2, Alcalá de Henares, 28801, Madrid, Spain

10

11 *Correspondence to:* Marco Girardello (marco.girardello@gmail.com), Gonzalo Oton (gonzalo.oton@ec.europa.eu)

12 * These authors contributed equally

13 **Abstract.** Forest structural diversity, defined as the heterogeneity of canopy structural elements in space, is an important axis
14 of functional diversity and is central to understanding the relationship between canopy structure, biodiversity, and ecosystem
15 functioning. Despite the recognised importance of forest structural diversity, the development of specific data products has
16 been hindered by the challenges associated with collecting information on forest structure over large spatial scales. However,
17 the advent of novel spaceborne LiDAR sensors like the Global Ecosystem Dynamics Investigation (GEDI) is now
18 revolutionising the assessment of forest structural diversity by providing high-quality information on forest structural
19 parameters with a quasi-global coverage. Whilst the availability of GEDI data and the computational capacity to handle large
20 datasets have opened up new opportunities for mapping structural diversity, GEDI only collects sparse measurements of
21 vegetation structure. Continuous information of forest structural diversity over large spatial domains may be needed for a
22 variety of applications. The aim of this study was to create wall-to-wall maps of canopy structural diversity in European forests
23 using a predictive modelling framework based on machine learning. We leverage multispectral and Synthetic Aperture Radar
24 (SAR) data to create a series of input features that were related to eight different structural diversity metrics, calculated using
25 GEDI. The models proved to be robust, indicating that active radar and passive optical data can effectively be used to predict
26 structural diversity. Our dataset finds applications in a range of disciplines, including ecology, hydrology, and climate science.
27 As our models can be regularly rerun as new images become available, it can be used to monitor the impacts of climate change
28 and land use management on forest structural diversity.

29

30 **1 Introduction**

31 Information on forest canopy structure is important for several disciplines, including Earth System Science, Ecology,
32 Hydrology, and Climate Science. Forest canopy structure plays a fundamental role in ecosystem functioning by affecting
33 carbon storage and cycling, regulating the hydrological cycle, and influencing local and regional climate patterns (Migliavacca
34 et al., 2021; Shugart et al., 2010; Sun et al., 2018). In addition, canopy structure is critical for maintaining high levels of
35 biodiversity by supporting a high diversity of ecological niches (Larue et al., 2019).

36

37 The concept of structural diversity or complexity, herein defined as the heterogeneity or variability of canopy structural
38 elements in vertical or horizontal space (Ehbrecht et al., 2021; Hakkenberg et al., 2023; LaRue et al., 2019), is central to
39 understanding the relationship between canopy structure, biodiversity, and ecosystem functioning. Structurally diverse forests
40 can host a wide variety of functionally complementary species, which tend to increase resource-use efficiency and promote
41 feedbacks that enhance resource availability (Gough et al., 2019; Murphy et al., 2022). As a result, these forests can capture
42 light more efficiently, leading to increased ecosystem productivity (Atkins et al., 2018; Toda et al., 2023). Therefore, the
43 availability of data on forest structural diversity over large spatial scales is critical for predicting and managing the response
44 of forest ecosystems to global change.

45

46 Mapping forest structural diversity over large spatial scales proved challenging due to the lack of comprehensive datasets and
47 consistent data collection methodologies, hindering our ability to predict ecosystem function at large geographic scales. Whilst
48 forest structural parameters can be measured in various ways, traditional field-based measures of stand structure are generally
49 labour-intensive and have been limited to small areas (Goodbody et al., 2023). Laser scanning, or LiDAR, has been proved a
50 sound alternative for measuring tree height from 3D data measured through echoes (Coops et al., 2021). However, data from
51 airborne LiDAR have been limited in spatial and temporal coverage to specific regions (Hancock et al., 2021). Recent advances
52 in satellite remote sensing technology and computational capabilities have made it possible to measure a range of structural
53 variables at larger scales than ever before. Notably, the Global Ecosystem Dynamics Investigation (GEDI) (Dubayah et al.,
54 2020a) instrument, placed on board the International Space Station (ISS) in December 2018, collecting LiDAR samples until
55 March 2023, has revolutionized the assessment of forest structure. Recent studies have shown how structural data collected by
56 GEDI can be used in several applications ranging from biomass estimation to the monitoring of biodiversity and ecosystem
57 disturbances (Crockett et al., 2023; Hakkenberg et al., 2023; Holcomb et al., 2024). These early examples demonstrate the
58 future potential of the GEDI mission.

59

60 Whilst the availability of GEDI data and the computational capacity to handle large datasets have opened up new opportunities
61 to map structural diversity, GEDI only collects sparse measurements of vegetation structure. Although the GEDI mission has
62 recently been extended, it is expected to cover only a minimal fraction of the land surface. Depending on the application of

63 interest, continuous information on structural diversity over forests may be needed. Combining GEDI with other types of
64 satellite remote sensing data within a machine learning framework may thus be necessary for the creation of structural diversity
65 data products that have continuous coverage and that extend beyond the timeframe covered by the GEDI mission. In this
66 context, predictor variables derived from complementary satellite observations are used to bridge the gap between sparse GEDI
67 measurements and the need for wall-to-wall maps of forest structural diversity. These predictors can act as observable proxies
68 for canopy structural complexity, enabling the spatial extrapolation of the GEDI-derived structural diversity metrics across
69 Europe. Several recent studies have successfully combined GEDI data with other remote sensing data sources to predict canopy
70 structure in areas not covered by GEDI, paving the way for mapping specific structural features of vegetation regionally and
71 globally (Aragoneses et al., 2024; Lang et al., 2023; Potapov et al., 2021; Schwartz et al., 2024). Additionally, preliminary
72 efforts to assess the potential of GEDI data to capture canopy diversity over different regions have been carried out (Schneider
73 et al., 2020). However, despite these significant advances, no efforts have been made to map forest structural diversity at a
74 continental scale in Europe.

75

76 To address the lack of readily available structural diversity data, we combined a suite of structural diversity indicators
77 calculated using GEDI data with active radar and passive optical data from the Sentinel-1, Sentinel-2, and ALOS-PALSAR
78 missions. This sensor combination was specifically selected to enable spatially and temporally consistent, wall-to-wall
79 estimates suitable for large-scale and monitoring, while capturing complementary structural information across different
80 canopy layers: Sentinel-2 multispectral data are sensitive to canopy biochemical and structural properties at the crown surface,
81 including vegetation density and phenological state. Sentinel-1 C-band SAR interacts primarily with the upper canopy and
82 smaller structural components, capturing variations in canopy roughness ALOS-PALSAR-2 L-band SAR, owing to its longer
83 wavelength, exhibits enhanced sensitivity to larger structural elements and sub-canopy features, providing information on
84 forest vertical complexity. These different sources of data were then integrated using a predictive modelling framework, based
85 on a machine learning method. The resulting models were used to predict structural diversity across Europe. Although Sentinel-
86 1, Sentinel-2 and ALOS-PALSAR-2 data have been previously used for predicting canopy height and other structural
87 components of forests, their joint use for mapping forest structural diversity has not yet been attempted (Liu et al., 2025; Wang
88 et al., 2024). Our analysis includes a total of eight structural diversity metrics, including metrics that quantify the vertical and
89 horizontal heterogeneity of the canopy, as well as metrics that quantify the heterogeneity of forest structure among GEDI
90 observations within a given area. The dataset presented here is readily available for use as input in various environmental
91 models and analyses.

92

93 **2 Methods**

94 We calculated eight forest structural diversity metrics using NASA GEDI observations (Dubayah et al., 2020b). A list of the
95 metrics is reported in Table 1. A machine learning (ML) framework was used to model the relations between each metric and

96 a series of predictors derived from passive optical and active radar remote sensing data. The model was then used to create a
97 structural diversity dataset that covers the whole forested domain of Europe, extending up to $\sim 52^\circ$ North, which corresponds
98 to the northern latitudinal limit of the GEDI mission. The creation of the dataset involved five main steps (Fig. 1): (i) satellite
99 remote sensing data pre-processing, (ii) structural diversity metric calculation (iii) model training, (iv) model validation, and
100 (v) prediction (Fig. 1). Data from GEDI, Sentinel 1 and 2, ALOS-Palsar-2 were pre-processed and downloaded from Google
101 Earth Engine (GEE), a cloud-based infrastructure that combines a multi-petabyte catalogue of satellite imagery and geospatial
102 datasets with planetary-scale analysis capabilities (Gorelick et al., 2017).

103

104 We used data covering forests that had remained ecologically stable, meaning they experienced no canopy loss, from 2000 to
105 2021, as identified through the Global Forest Change product by Hansen et al. (2013). Furthermore, our analyses were limited
106 to areas where tree cover exceeded 30% and which bordered at least 6 out of 8 neighbouring pixels, also with tree cover
107 exceeding 30%. While our threshold is more stringent than Food and Agriculture Organization (FAO) definition of forest
108 (FAO, 2000), which specifies an area spanning more than 0.5 hectares with trees taller than 5 metres and a canopy cover of
109 more than 10%, it was chosen to capture areas with substantial arboreal density. Although our selection was guided by the
110 FAO's broader forest criteria, we customized these guidelines to suit our research focus. This threshold was intentionally
111 adopted to focus on landscapes with well-developed and spatially continuous forest canopies. This more conservative threshold
112 reduces the influence of sparsely treed or transitional land-cover types and improves the robustness and interpretability of
113 GEDI-based structural diversity metrics

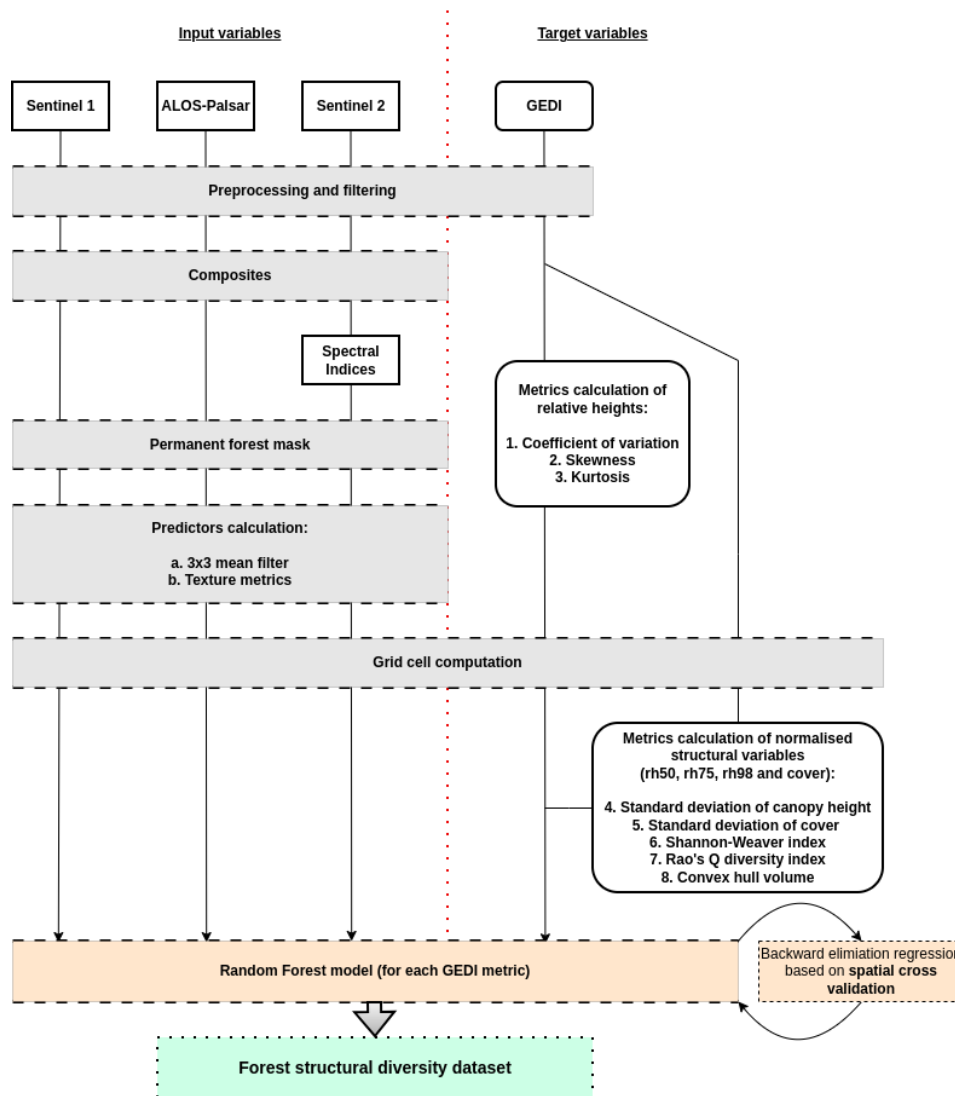
114

115 **2.1 Structural diversity metrics**

116 Structural diversity can be characterized in a variety of ways depending on the data from which it is calculated and the intended
117 application. In this work we adopted the common definition where diversity is defined in the vertical dimension as
118 heterogeneity of vegetation height and in the horizontal dimension as canopy heterogeneity (Hakkenberg and Goetz, 2021).
119 We chose a set of metrics that would characterize the heterogeneity within and among structural features for a given area,
120 reflecting both local (alpha) and regional (beta) measures of structural diversity. These complementary metrics have been
121 demonstrated to be particularly crucial for predicting tree diversity and ecosystem functioning (Coverdale and Davies, 2023;
122 Ma et al., 2022; Zhai et al., 2024). A summary of the metrics with the input data used is reported in Table 1. Several GEDI,
123 including Foliage Height Diversity (FHD from the GEDI L2B product) and the Waveform Structural Complexity Index
124 (WSCSI, from the GEDI L4C product), already capture important aspects of forest structural heterogeneity and have proven
125 highly valuable for large-scale analyses. However, recent work has shown that these indices exhibit strong scaling relationships
126 with top-of-canopy height (RH98) (de Conto et al., 2024).

127

128



130

131 Figure 1. General workflow employed in the creation of the forest structural diversity dataset. The workflow is segmented by a red dashed
 132 line, delineating the Remote Sensing predictors from the inputs to the target GEDI data. Boxes with solid edges represent the data that were
 133 directly utilised to train the Random Forest models. The grey boxes indicate the preliminary steps undertaken before the model training
 134 phase. The process culminates with orange boxes, which signifies the development of the predictive model itself, leading to the green box
 135 that represents the final output outcome—the forest structural diversity dataset.

136

137 In the context of this study, our objective was therefore not to directly use existing GEDI products as target variables, but to
 138 develop structural diversity metrics that explicitly quantify heterogeneity while minimising direct dependence on canopy
 139 height. This motivated the selection of eight complementary metrics based on the distributional properties of GEDI relative

140 height profiles and canopy cover, ecologically interpretable, minimally redundant with each other and with height, and suitable
141 for spatial aggregation and wall-to-wall mapping using multi-sensor satellite data.
142 The eight structural diversity metrics were designed to span three complementary dimensions of forest structural diversity
143 (Table 1). Vertical heterogeneity within individual canopy profiles is characterised using distributional metrics derived from
144 GEDI relative height profiles, namely the coefficient of variation, skewness, and kurtosis, which capture differences in vertical
145 layering and profile shape. Horizontal heterogeneity is described by the variability among GEDI observations within a spatial
146 unit, quantified through the standard deviation of canopy height (CH) and canopy cover (CC), reflecting spatial variation in
147 canopy structure across the landscape. Finally, combined structural diversity is represented using multivariate metrics
148 (Shannon index (SW), Rao's quadratic entropy (RAO), and convex hull volume (CVH)), which synthesize information from
149 multiple GEDI measurements into a single integrated index per spatial unit. Together, these metrics provide an interpretable
150 yet comprehensive characterisation of forest structural diversity while minimising redundancy among metrics and with top-
151 of-canopy height.
152

153 **2.1.1 GEDI input data and general framework**

154 GEDI data are collected from a full waveform LiDAR sensor operating onboard the International Space Station (ISS) from
155 April 2019 until January 2023. Due to the orbital path of the International Space Station (ISS), GEDI's coverage is primarily
156 limited to latitudes between $\sim 50^\circ$ North and south. The instrument provides sparse measurements (hereinafter sample plots or
157 shots) of vegetation structure over an area defined by a sampling footprint of about 25 m diameter.
158

159 Input data included the GEDI Level 2A Relative Heights (RH), and the Level 2B total Canopy Cover (CC) values (see Table
160 1). In the literature, rh^{98} is taken as a reference for the top canopy height (CH) (Lang 2022), CC is the proportion of the shot
161 covered by the vertical projection of the tree crowns. The GEDI data were downloaded from Google Earth Engine after
162 applying a filtering procedure to remove low-quality and unreliable observations and to reduce noise in the input data, based
163 on standard GEDI quality flags and thresholds (Table S1 in the Supplement).

164 Structural diversity metrics were computed for each spatial analysis unit, defined as regular grid cells (hereafter referred to
165 pixels) at 1 km, 5 km, and 10 km spatial resolution. For each pixel, all number (M) of valid GEDI shots overlapping the pixel
166 between April 2019 and January 2023 were collected. The structural diversity metrics of a given pixel are calculated by
167 aggregating all M overlapping that pixel. Each GEDI shot i was characterized by its RH distribution $RH_i =$
168 $\{rh_i^k, rh_i^{k+1}, \dots, rh_i^{100}\}$ with $k: rh_i^k \geq 0$ (i.e. only the positive values were considered) and total canopy cover cc_i . To ensure
169 robust estimation of structural diversity, pixels with fewer GEDI observations than a minimum sampling threshold were
170 excluded. This threshold was defined as the median number of valid GEDI shots across all pixels at a given spatial resolution.
171 In addition, extreme metric values were filtered using a z-score criterion, with values exhibiting a deviation greater than 3

172 across pixels discarded as outliers. The remaining pixels were then used to compute the structural diversity metrics. A post-
173 processing step was applied to remove extreme values: pixels with structural diversity values exhibiting a z-score greater than
174 3 were discarded as outliers.

175 We computed the eight structural diversity metrics at three spatial resolutions (1 km, 5 km, and 10 km) using grids in the
176 Lambert Azimuthal Equal Area (LAEA) projection. The choice of these spatial resolutions reflects a trade-off between spatial
177 detail, GEDI sampling density, and metric robustness. Because GEDI provides sparse footprint-level measurements, reliable
178 estimation of structural diversity requires a sufficient number of observations within each spatial unit. Coarser resolutions
179 improve metric stability, while finer resolutions provide greater spatial detail at the cost of higher uncertainty. The 10 km
180 resolution was identified as the most robust scale for continental-scale analyses and is compatible with the spatial aggregation
181 typically used in regional ecosystem and Earth system models. The 5 km and 1 km products support applications requiring
182 finer spatial detail, such as regional ecological analyses and biodiversity assessments. We acknowledge that applications
183 focused on small-scale disturbances, edge effects, or forest fragmentation would benefit from even finer resolution; however,
184 at such scales, the limited density of GEDI observations substantially constrains reliable metric estimation over large areas.

185

186 In the following sections, we detail the methodology employed for calculating the diversity metrics and predictor variables,
187 which makes use of the mean $\mu(X)$, standard deviation $\sigma(X)$, skewness $\gamma(X)$, excess kurtosis $\kappa(X)$, coefficient of variation
188 $cv(X)$ of a variable $X = \{x_1, \dots, x_M\}$, where X represents a vector of observations (see Appendix A for the explicit
189 formulations).

190

191 **2.1.2 Vertical Diversity Metrics**

192 RH metrics provide information on the vertical distribution of the plant elements, that is, the vertical profile (VP) of the
193 vegetation (see Fig. S1 in the Supplement). The VP in a sample can be reconstructed from the corresponding RH distribution,
194 and the profile's moments (i.e. mean, standard deviation, skewness, kurtosis) are well approximated by the RH distribution's
195 moments (Fig. S1 in the Supplement).

196

197 The following calculated indicators characterise the heterogeneity of the vertical profile:

- 198 1. the average coefficient of variation of the vertical profiles

199

$$\tau_{CV} = \mu(CV)$$

200 with $CV = \{cv(RH_1), \dots, cv(RH_M)\}$. The coefficient of variation $cv(RH)$ quantifies the extent of vertical variability in relation
201 within a vertical profile as the ratio between the standard deviation and the mean of the relative height distribution. τ_{CV}
202 therefore indicates greater vertical dispersion relative to mean profile height and hence greater vertical heterogeneity;

203

204 2. the average skewness of the vertical profiles

$$205 \tau_{SK} = \mu(\Gamma)$$

206 where $\Gamma = \{\gamma(RH_1), \dots, \gamma(RH_M)\}$. represents the set of skewness values computed from the RH distribution of each of the
207 M GEDI observations within the pixel. Skewness $\gamma(RH)$, or third standardized moment, is a measure of the asymmetry of the
208 VP about its mean, and it can be positive, negative, or zero (Fig. S2, a and d panels in the Supplement). If VP is a unimodal
209 distribution (a distribution with a single peak), positive skewness generally indicates an asymmetric tail extending toward
210 larger height values (overstorey heterogeneity), while negative skewness suggests a tail extending toward smaller height values
211 (understorey heterogeneity). However, note that in the cases where one tail is long, but the other tail is fat, or the distribution
212 is multi-modal, skewness does not always obey this simple rule.

213

214 3. the average excess kurtosis of the vertical profiles

$$215 \tau_{KU} = \mu(K)$$

216 where $K = \{\kappa(RH_1), \dots, \kappa(RH_M)\}$ represents the set of excess kurtosis values computed from the RH distribution of each of
217 the M GEDI observations within the pixel. Excess $\kappa(RH)$ is a measure of the "tailedness" of the VP, and it is equal to 0 for
218 any univariate normal distribution, (Fig. S2 a and d panels in the Supplement). Distributions with negative/positive excess
219 kurtosis are said to be platykurtic/leptokurtic. Platykurtic distributions show fewer and/or less extreme outliers than the normal
220 distribution. In this case, the vegetation mass is more concentrated around the VP mean than near the vertical extremes (i.e.
221 the ground and to top canopy height). However, it is important to note that while kurtosis, the fourth moment, does play a role
222 in characterizing the shape of VP, its influence is comparatively smaller than that of the standard deviation, the second moment,
223 and skewness, the third moment. For instance, two distinct VPs may exhibit identical excess kurtosis while displaying
224 markedly disparate distributions in terms of standard deviations.

225

226 2.1.3 Horizontal Diversity Metrics

227 We calculated 5 vertical horizontal diversity indices.

228

229 1. the standard deviation of the canopy heights

$$230 \tau_{CH} = \sigma(CH)$$

231 where $CH = \{rh_1^{98}, \dots, rh_M^{98}\}$ represents the set of rh^{98} values within the τ_{CH} . τ_{CH} indicates the spread of the canopy heights
232 in the area.

233

234 2. the standard deviation of the total canopy cover

$$235 \tau_{CC} = \sigma(CC)$$

236 where $CC = \{cc_1, \dots, cc_M\}$ represents the set of canopy cover values within the pixel. τ_{CC} indicates the spread of the total
 237 canopy cover in the area.

238

239 2.1.4 Combined Vertical and Horizontal and Diversity Metrics

240

241 3. the Shannon-Weaver index

242

$$243 \tau_{SW} = - \sum_{\log p_{\varepsilon\pi o\omega}} p_{\varepsilon\pi o\omega} \log p_{\varepsilon\pi o\omega}$$

244

245

246 in a 4D cartesian space defined on the basis $(rh^{50}, rh^{75}, rh^{98}, cc)$, where $p_{\varepsilon\pi o\omega}$ is the fraction of the GEDI samples within
 247 the pixel falling in a specific bin (see Appendix A2). We used a 5-unit bin size on each axis, and the GEDI CC values were
 248 amplified by 10. τ_{SW} measures the uncertainty or disorder inherent to the variable's possible outcomes. $\tau_{SW} = 0$ when all
 249 observations are confined within a single bin, otherwise τ_{SW} is larger than zero. Higher values indicate heterogeneity, while
 250 lower values suggest homogeneity.

251

252 4. Rao's quadratic diversity index

$$253 \tau_{RAO} = \sum_{\varepsilon\pi o\omega} \sum_{\varepsilon'\pi'o'\omega'} p_{\varepsilon\pi o\omega} D_{\varepsilon\pi o\omega}^{\varepsilon'\pi'o'\omega'} p_{\varepsilon'\pi'o'\omega'}$$

254 in the 4D cartesian space defined on the basis $(rh^{50}, rh^{75}, rh^{98}, cc)$, where $p_{\varepsilon\pi o\omega}$ is the fraction of the GEDI samples within
 255 the pixel falling in a specific bin and $D_{\varepsilon\pi o\omega}^{\varepsilon'\pi'o'\omega'}$ the cartesian distance between two bins (see Appendix A2). We used a 1-unit
 256 bin size on each axis, and the GEDI CC values were amplified by 10. τ_{RAO} ranges from zero, indicating no diversity, to positive
 257 numbers. Differently from τ_{SW} index, τ_{RAO} considers both abundance ($p_{\varepsilon\pi o\omega}$ terms) and dissimilarity in the sampled data
 258 ($D_{\varepsilon\pi o\omega}^{\varepsilon'\pi'o'\omega'}$ term).

259

260 5. convex hull volume

261

$$\tau_{CVH} = CVH(SHT)$$

262 in the 4D cartesian space defined on the basis $(rh^{50}, rh^{75}, rh^{98}, cc)$. We used a 1-unit bin size on each axis, and the GEDI
 263 CC values were amplified by 10. CVH is the function calculating the convex hull volume on the ensemble $SHT =$
 264 $\{sht_1, \dots, sht_M\}$, with $sht_i = (rh_i^{50}, rh_i^{75}, rh_i^{98}, cc_i)$. Larger volumes indicate increased heterogeneity.

265

266 Table 1. Structural diversity metrics computed in this study.

267

Metric	Description	Units	GEDI data	Diversity
τ_{CV}	VP coefficient of variation	-	RH	vertical
τ_{SK}	VP skewness	-	RH	vertical
τ_{KU}	VP excess kurtosis	-	RH	vertical
τ_{CH}	CH standard deviation	m	rh^{98}	horizontal
τ_{CC}	CC standard deviation	-	cc	horizontal
τ_{SW}	Shannon-Weaver index	-	$(rh^{50}, rh^{75}, rh^{98}, cc)$	combined
τ_{RAO}	Rao's quadratic entropy index	-	$(rh^{50}, rh^{75}, rh^{98}, cc)$	combined
τ_{CVH}	Convex Hull volume	-	$(rh^{50}, rh^{75}, rh^{98}, cc)$	combined

268

269 **2.2 Predictor variables**

270 The variables used as ML predictors were calculated from Sentinel-1, Sentinel-2, and ALOS-PALSAR-2 observed data, which
 271 provide complementary information on forest canopy structure derived from optical reflectance, C- and L-band SAR
 272 backscatter, and associated textural properties. The predictor calculation involved the following steps:

- 273 1. appropriate bands/indices ϕ_α were calculated from the remote sensing raster images;
- 274 2. the $\phi_{\alpha,i}^\beta$ values, with β equal to SM, ASM, ENT, or DISS, are calculated from the pixels within the 7×7 window
 275 aligned with the footprint of the GEDI shot i . $\phi_{\alpha,i}^{SM}$ is the spatial mean. $\phi_{\alpha,i}^{ASM}$, $\phi_{\alpha,i}^{ENT}$, and $\phi_{\alpha,i}^{DISS}$ are the texture metrics
 276 Angular Second Moment (ASM), entropy, and dissimilarity index, respectively (see Appendix A3).
- 277 3. the raster images of the predictors were computed as $\phi_\alpha^\beta = \mu(\Phi_\alpha^\beta)$, where the mean is calculated on the M values
 278 $\Phi_\alpha^\beta = \{\phi_{\alpha,1}^\beta, \dots, \phi_{\alpha,M}^\beta\}$ corresponding to the geographical positions that overlap the image pixels.

279 In the following, we present what satellite remote sensing data were used and how they were combined for the calculation of
 280 the indices. A total of 47 predictors were derived. A summary of the predictors is reported in Table S2 in the Supplement.

281

282 **2.2.1 Sentinel-1 radar data**

283 The European Space Agency's (ESA) Sentinel-1 (S1) comprises a constellation of two polar-orbiting satellites, sun-
 284 synchronous orbit with a 12-day repeat cycle, which operate day and night a C-band ($\lambda = 5.5$ cm) Synthetic Aperture Radar
 285 (SAR) to capture data at a spatial resolution of approximately 10 meters. The radar enables the acquirement of imagery

286 regardless of the weather, and the C-band frequency is particularly effective in interacting with fine vegetative elements such
 287 as leaves and branches (Naidoo et al., 2015). In our study, from Sentinel-1 we utilized both backscatter and coherence data.
 288 Backscatter is the portion of the outgoing radar signal that the target redirects directly back towards the radar antenna. The
 289 backscatter characteristics provide crucial insights into the physical properties of forest canopies. For the year 2020, we focused
 290 on the signal dual-polarization VV and VH Sentinel-1A (S1A) and Sentinel-1B (S1B) Ground Range Detected (GRD) data,
 291 acquired in the Interferometric Wide (IW) swath mode, as it predominantly covers land masses (Kellndorfer et al., 2022).
 292 VV(H) is a mode that transmits vertical waves and receives vertical (horizontal) waves to create the SAR image. We selected
 293 data from the descending orbit, which has been shown to exhibit fewer correlations with evapotranspiration (ET) (Mueller et
 294 al., 2022). Sentinel-1 data used in this study were obtained from Google Earth Engine, where they had already undergone some
 295 pre-processing. Preprocessing steps carried out by the Google Earth Engine team include applying the orbit file for geocoding,
 296 removing GRD border noise and thermal noise, and performing radiometric calibration. We performed a radiometric terrain
 297 correction following (Vollrath et al., 2020), as well as the removal of stripes and edges. Following radiometric terrain
 298 correction and the removal of stripes and edge artefacts, we selected all valid Sentinel-1 observations captured over Europe
 299 within a six-month window centred on the date of maximum NDVI identified independently for each pixel from the Sentinel-
 300 2 dataset (see Section 2.2.3). We then derived:

- 301 1. the S1 backscatter six-month mean $\phi_{S1VVgs\mu}$ and $\phi_{S1VHgs\mu}$, where the mean is intended to mitigate speckle noise
 302 while emphasizing the vegetation growing season;
- 303 2. the S1 backscatter standard deviation growing season $\phi_{S1VVgs\sigma}$ and $\phi_{S1VHgs\sigma}$;
- 304 3. the S1 backscatter bi-monthly mean $\phi_{S1VVpre\mu}$ and $\phi_{S1VHpre\mu}$ for a window extending two months before the month
 305 before the peak, $\phi_{S1VVact\mu}$ and $\phi_{S1VHact\mu}$ for the period spanning one month before to one month after the peak, and
 306 $\phi_{S1VVpost\mu}$ and $\phi_{S1VHpost\mu}$ for the two months after the month after the peak.

307 Coherence is the relationship between waves in a beam of electromagnetic (EM) radiation. Two wave trains of EM radiation
 308 are coherent when they are in phase. In radar, the term coherence is also used to describe systems that preserve the phase of
 309 the received signal. Coherence measurements serve as a valuable tool for monitoring temporal changes in forested
 310 environments (Bruggisser et al., 2021; Cartus et al., 2022). The coherence data utilized in this study were extracted from the
 311 dataset developed by Kellndorfer et al. (2022). This dataset is the product of multi-temporal, repeat-pass interferometric
 312 processing of S1 SAR images. It incorporates signal dual-polarization VV and VH data from S1A and S1B in Single Look
 313 Complex (SLC) format, utilizing the IW swath mode from the year 2020. The product is divided into seasonal sets, and we
 314 selected summer (June-August) coherence metrics ϕ_{CO} , aligned with the growing season, employing a 12-day repeat-pass
 315 interval to optimize the balance between image continuity and temporal resolution. This interval was chosen to minimize gaps
 316 in the image series, compared to shorter intervals (such as 6 days), while longer intervals (e.g., 18, 24, 36, or 48 days) could
 317 result in excessive decorrelation. With a relatively unchanged scene between acquisitions, higher coherence values are

318 achieved, which correlate strongly with the radar signal and hence, reduce noise levels. Furthermore, we prioritized signal VV
319 polarization to enhance our understanding of the data, as it minimizes vegetation decorrelation effects (Pan et al., 2022)

320

321 **2.2.2 ALOS-PALSAR-2 radar data**

322

323 The ALOS-PALSAR-2 (Advanced Land Observing Satellite - Phased Array type L-band Synthetic Aperture Radar) system,
324 developed by the Japan Aerospace Exploration Agency (JAXA), operates in the L-band frequency ($\lambda = 23.62$ cm) at a spatial
325 resolution of 25 meters. The L-band is particularly effective at penetrating canopy layers to provide backscatter signals from
326 larger vegetative features such as branches and trunks, and even from the ground. For our analysis, we made use of the global
327 mosaic of backscatter annual composites, which incorporate signal dual-polarization HH and HV data (Shimada et al., 2014)
328 from the years 2019 and 2020, accessed via GEE. In instances where the data availability was constrained for an annual
329 composite, the dataset was supplemented with observations from adjacent years. To ensure the reliability of our dataset and
330 account for possible gaps in observations, we averaged data across two years to generate $\phi_{AP2HH\mu}$ and $\phi_{AP2HV\mu}$ data. This
331 approach helps mitigate noise and stabilize the composite images.

332

333 **2.2.3 Sentinel-2 optical data**

334 The ESA Sentinel-2 (S2) mission comprises a constellation of two polar-orbiting satellites placed in the same sun-synchronous
335 orbit, phased at 180° to each other. Its high revisit time (10 days at the equator with one satellite, and 5 days with 2 satellites
336 at best) allows monitoring of the Earth's surface changes. The Multi-Spectral Instrument (MSI) on board the 2 platforms
337 collects the sunlight reflected from the Earth and supplies high-resolution multispectral imagery with resolutions of 10 and 20
338 meters. Data are acquired at 10 m spatial resolution for Visible (Blue, Green, Red) and Near-Infra-Red (NIR) bands, and at 20
339 m spatial resolution for VNIR-Red Edge (RE1, RE2, RE3, RE4) and Short Wave Infra-Red (SWIR) bands (SWIR1, SWIR2).
340 The Level-2A product provides atmospherically corrected Surface Reflectance (SR) images. In this study we used all the
341 Level-2A images from 2000 to 2021 identified by a scene-level cloud and snow cover smaller than 70% and 5%, respectively,
342 as provided by Google Earth Engine. We then calculated:

- 343 1. the Normalized Difference Vegetation Index

344

$$\phi_{NDVI} = \frac{\rho_{NIR} - \rho_{Red}}{\rho_{NIR} + \rho_{Red}}$$

345 as proposed by (Rouse et al., 1974) it is a widely recognized index strongly correlated with vegetation health and primary
346 productivity;

- 347 2. the Normalized Difference Water Index

348

$$\phi_{NDWI} = \frac{\rho_{NIR} - \rho_{SWIR1}}{\rho_{NIR} + \rho_{SWIR1}}$$

349 as proposed by (Gao, 1996), it is correlated with leaf water content.

350 3. the Normalized Difference Red Edge Index

351
$$\phi_{NDRE} = \frac{\rho_{NIR} - \rho_{RE1}}{\rho_{NIR} + \rho_{RE1}}$$

352 as proposed by Gitelson and Merzlyak, (1994) it offers sensitivity to chlorophyll content and is useful in assessing forest
353 composition and canopy cover;

354 4. the Modified Soil Adjusted Vegetation Index

355
$$\phi_{MSAVI} = \frac{2 \cdot \rho_{NIR} + 1 - \sqrt{(2 \cdot \rho_{NIR} + 1)^2 - 8 \cdot (\rho_{NIR} - \rho_{Red})}}{2}$$

356 as proposed by (Qi et al., 1994), it is suited to monitoring vegetation density and dynamics, particularly during early growth
357 stages when bare soil is prevalent, thereby minimizing soil background effects;

358 5. the Green Normalized Difference Vegetation Index

359
$$\phi_{GNDVI} = \frac{\rho_{NIR} - \rho_{Green}}{\rho_{NIR} + \rho_{Green}}$$

360 as proposed (Gitelson and Merzlyak, 1998), it responds to chlorophyll concentration and is indicative of vegetation
361 composition, structure, habitat conditions, and species diversity;

362 6. the standard deviation of NDVI

363
$$\phi_{NDVI\sigma} = \sigma(\phi_{NDVI})$$

364 as noted by (Perrone et al., 2024), it accounts for a significant portion of the variability observed in-situ plant diversity.

365

366 **2.3 Model training and validation**

367 We used a machine learning method - Random Forest (Breiman, 2001) - to quantify the relations between the remote sensing
368 predictors and the eight metrics. Random Forest is an ensemble learning method based on decision trees that is widely
369 employed for regression tasks. A key advantage of Random Forests is that model fitting is relatively fast and hyperparameter
370 optimization requires only a moderate amount of tuning, compared to other machine learning methods. Optimization of the
371 Random Forest model typically involves tuning a number of hyperparameters. These include the size of the forest (i.e. the
372 number of decision trees), the method of bootstrapping samples, and the setting of the maximum depth for the trees. We
373 specified a fixed number of trees, 600; bootstrapping, a technique that involves random sampling with replacement, which
374 contributes to the diversity of the decision trees in the model and helps prevent overfitting; and we did not impose any
375 limitations on the depth of the individual decision trees, allowing them to expand fully. To evaluate the performance of the
376 Random Forest model, we used mean squared error (MSE) as the metric.

377 To mitigate the potential for overfitting, we used a backward stepwise selection process that begins with a full model including
378 all available predictors. The algorithm then iteratively removes the least important feature, as determined by its contribution
379 to model performance. The relative importance of predictors was assessed using a permutation procedure (Altmann et al.,
380 2010). At each iteration, the model complexity is reduced by one predictor, and the resulting model is evaluated. We compared

381 each newly simplified model to the immediate predecessor to determine whether there was an improvement in performance or
382 a decrease that was less than 1% worse. The elimination process is halted if the removal of additional predictors causes the
383 model's performance to decrease by more than 1% compared to the previous iteration. At each step, a spatial cross-validation
384 procedure is used to assess the performance of the model. The metric we utilized to assess model performance throughout this
385 process was the coefficient of determination (R^2).

386 To validate the reduced models, we used two types of validation techniques to assess their predictive accuracy and robustness:

- 387 • Random train-validation split: in this approach, the dataset was randomly split, allocating 33% for model validation.
388 Random validation is a common method that provides a quick and often effective means of evaluating model
389 performance on unseen data. However, it has a notable drawback when dealing with spatial data: it disregards the
390 spatial structure inherent in the dataset (i.e. points close to each other are, generally, more similar than points further
391 away). By ignoring this spatial autocorrelation, random validation may inadvertently conceal overfitting issues,
392 leading to an overly optimistic perception of the model's predictive capabilities.
- 393 • 10-Fold Spatial Cross-Validation (Roberts et al., 2016): we implemented a 10-fold spatial cross-validation procedure
394 to address the shortcomings of random validation, thus reducing the overfitting. This more sophisticated method
395 partitions the data into ten spatially distinct subsets, or folds, ensuring that each fold comprises disjointed sets that are
396 geographically separated. The partitioning is achieved by clustering data points according to their spatial coordinates,
397 which preserves the spatial structure and autocorrelation present in the dataset. During the validation process, each
398 fold is used once as a validation set while the remaining folds serve as the training set. This technique provides a more
399 realistic evaluation of the model's performance and its ability to generalize across different spatial regions, thereby
400 offering a safeguard against overfitting and ensuring a more reliable assessment of the model's true predictive power.

401 Both validation approaches were retained because they address complementary evaluation objectives. Spatial cross-validation
402 provides a conservative assessment of model generalisation in the presence of spatial autocorrelation and is therefore more
403 appropriate for evaluating transferability across regions. Random validation, while potentially optimistic for spatial data, was
404 included to facilitate comparison with previous studies that rely on this approach and to characterise overall model behaviour
405 under standard machine-learning evaluation settings. Throughout the manuscript, spatial cross-validation results are
406 emphasised when discussing model robustness and applicability.

407 Models were fitted to datasets created at different resolutions including data calculated at 10 km, 5 km and 1 km. Prediction
408 uncertainty was quantified by calculating the standard deviation of predictions across the ensembles of decision trees in the
409 Random Forest models. This metric captures the variability in predictions among individual trees within each model, providing
410 a measure of uncertainty associated with predictions for the different response variables.

411
412
413

414 **3 Results**

415

416 **3.1 Spatial patterns of forest structural diversity**

417

418 The dataset includes spatial grids for eight structural diversity metrics at three different resolutions (10 km, 5km and 1 km).

419 These metrics show a significant variation in structural diversity across the European forests as shown in Fig. 2 (see also Fig.

420 S3 and Fig. S4 in the Supplement for 5km and 1km resolution datasets).

421

422 An examination of the variability in the 10 km resolution metrics in climate space revealed distinct patterns along temperature

423 and precipitation gradients (Fig. 3). Patterns of variability in metrics describing vertical heterogeneity showed significant

424 differences when comparing the coefficient of variation (τ_{CV}) and skewness (τ_{SK}) against kurtosis (τ_{KU}). The coefficient of

425 variation and skewness primarily exhibited high values at the extremes of the climatic gradient. This is observed in warm and

426 arid climates where total annual precipitation is below ~ 500 mm and Annual Mean Temperature is above ~ 10 °C, as well as

427 in colder climates where Annual Mean Temperature is below ~ 5 °C. Patterns of variability in the kurtosis were more nuanced,

428 consistently showing negative values across the European domain, which suggests a tendency for a platykurtic distribution in

429 the vertical profile of canopies under diverse environmental conditions. The most pronounced negative kurtosis values were

430 observed for the northern part of the temperate climate zone (Fig. 3). By contrast, more heterogeneous patterns occurred in

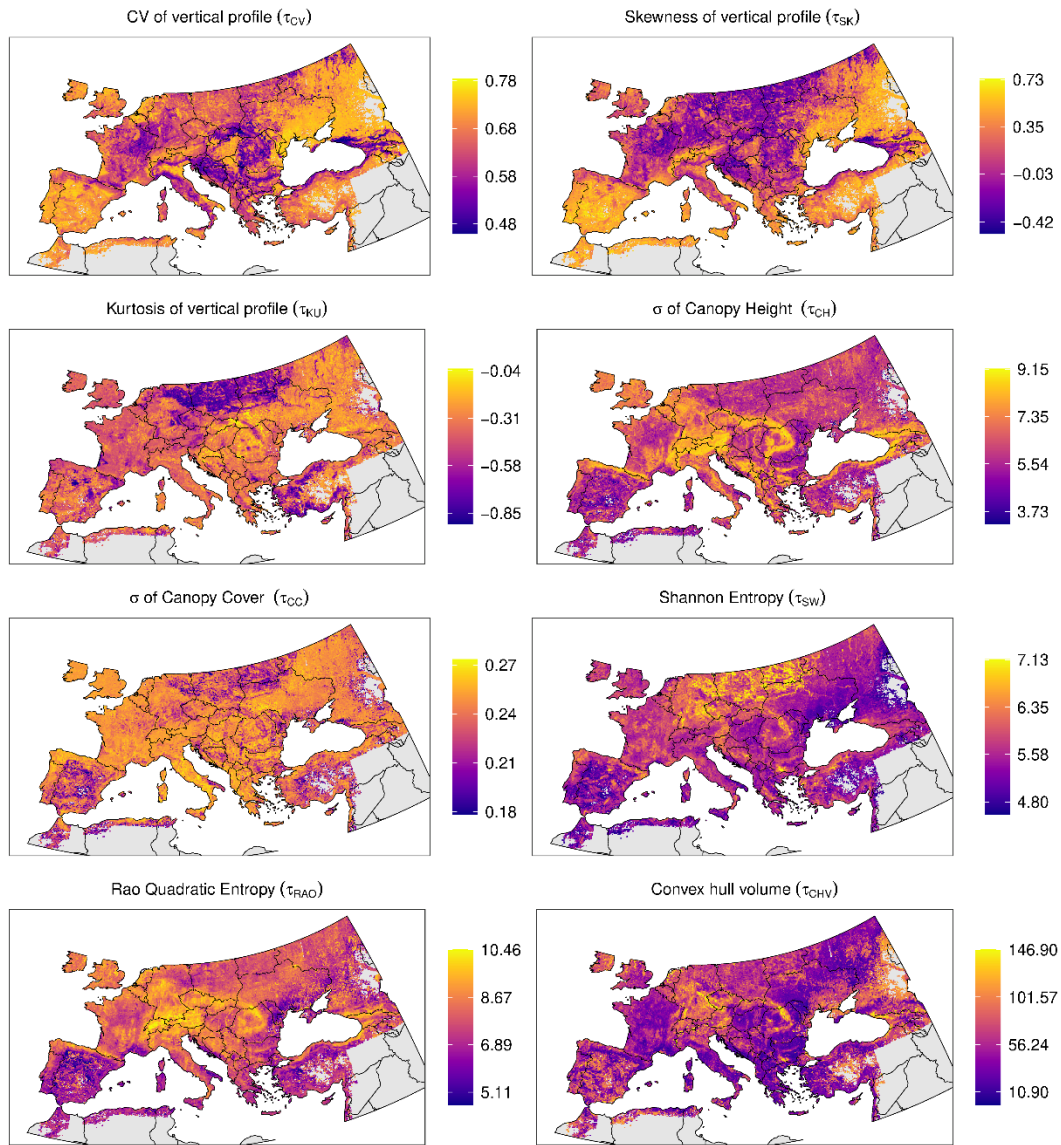
431 other areas such as those with a Mediterranean climate, showing high variability (Fig. 3). Diversity metrics describing

432 structural heterogeneity in horizontal space, as well as combined metrics, (τ_{CH} , τ_{CC} , τ_{SW} , τ_{RAO} , τ_{CVH}) also showed

433 considerable variability along precipitation and temperature gradients. With the exception of the convex hull (τ_{CVH}), all metrics

434 displayed low diversity values in hot and dry climates.

435



436

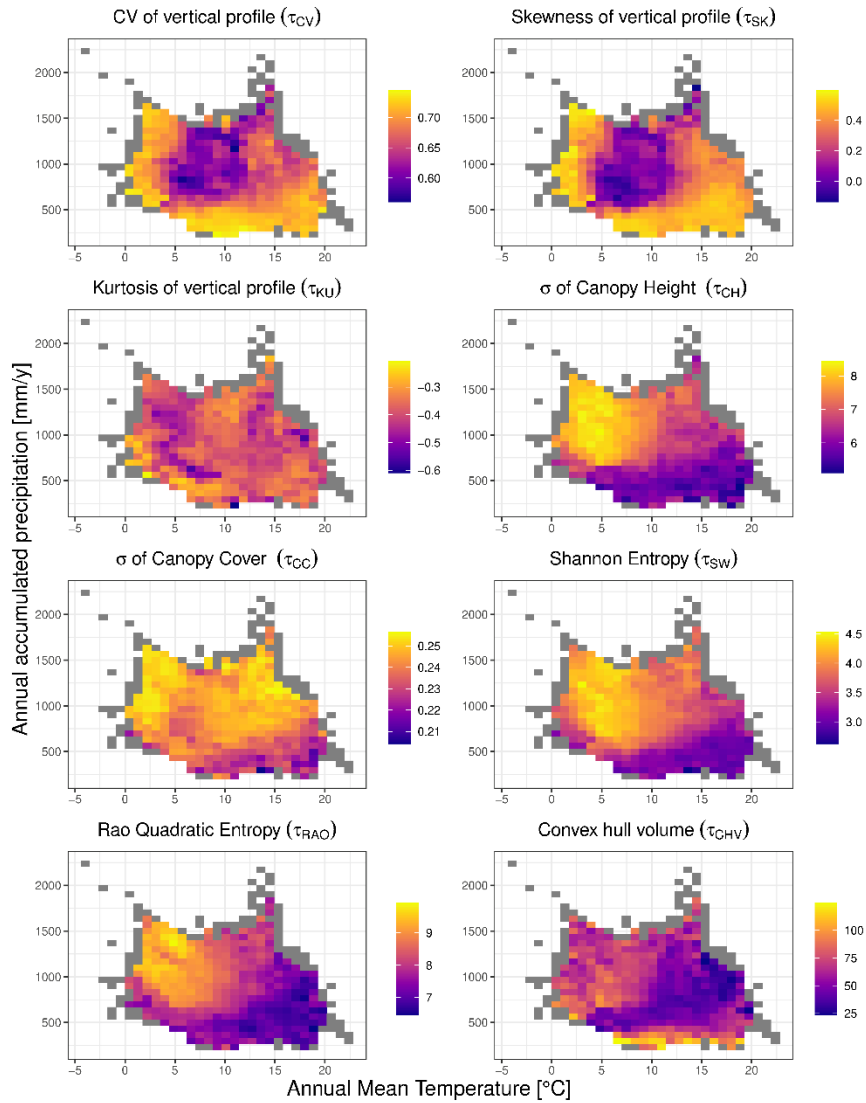
437

438 Figure 2. Mapped structural diversity at a 10 km resolution, derived from the Random Forest modelling. Each panel illustrates the geographic distribution of
 439 a specific metric (see methods for metric details). The colour palette transitions from purple to yellow, denote an increasing gradient of structural diversity,
 440 with warmer colours signifying higher values.

441

442

443



444

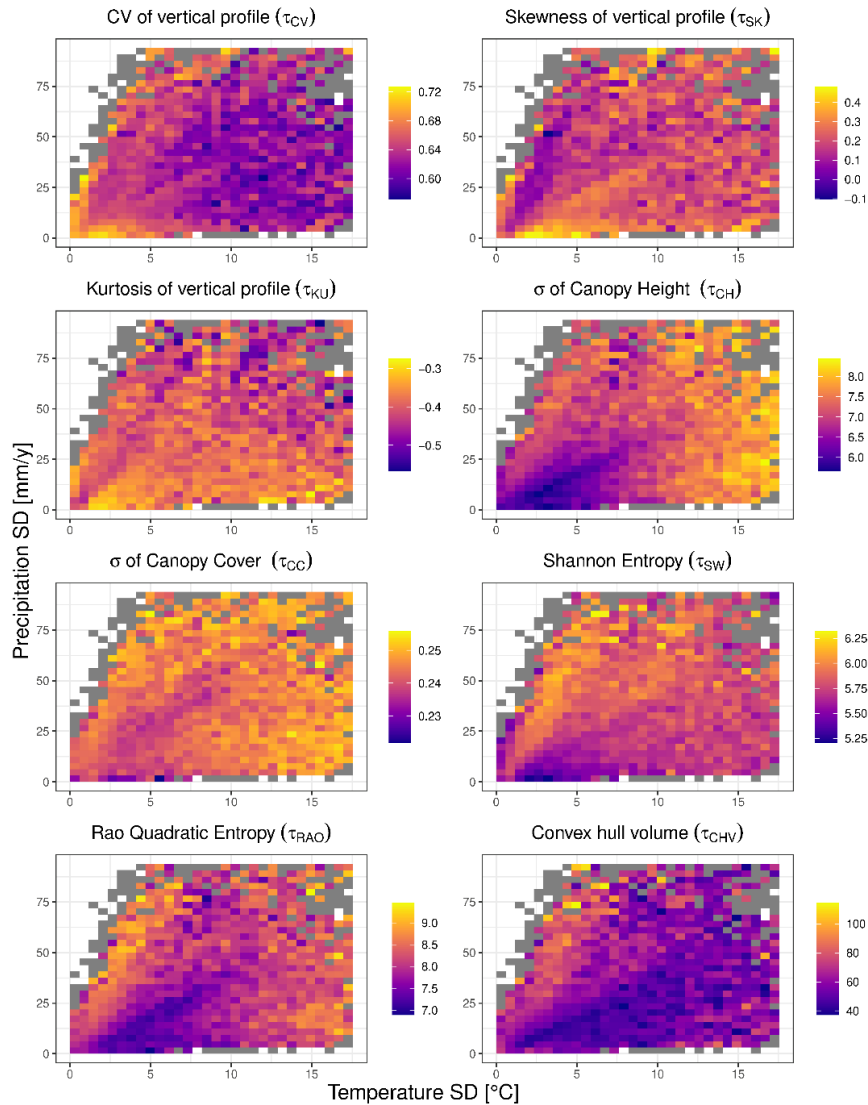
445 Figure 3. Structural diversity variables mapped against mean climate (temperature and precipitation). The results refer to the dataset at 10 km resolution.

446 Coloured bins depict variation in structural diversity, calculated as the average of the structural diversity values falling within each bin. Grey bins indicate

447 those containing fewer than 5 observations, for which the average was not calculated.

448

449



450

451 Figure 4. Structural diversity variables mapped against climate variability (temperature and precipitation SD in space). The results refer to the dataset at 10
 452 km resolution. Coloured bins depict variation in structural diversity, calculated as the average of the structural diversity values falling within each bin. Grey
 453 bins indicate those containing fewer than 5 observations, for which the average was not calculated.

454

455

456 Specifically, a combination of precipitation levels below ~ 500 mm and annual mean temperatures above $\sim 10^\circ\text{C}$ (Fig. 3) was
 457 associated with the lowest levels of diversity. By contrast, the highest levels of diversity generally occurred in areas with higher
 458 precipitation levels (> 500 mm). Patterns of variability in the metrics in climate space for 5km and 1 km resolution (see Fig.
 459 S5 and Fig. S6 in the Supplement) dataset were broadly concordant with the 10km dataset, indicating that the results are
 460 insensitive to the grain size at which they were calculated.

461 An examination of the 10 km resolution structural diversity metrics along gradients of temperature and precipitation variability
462 (Fig. 4) revealed distinct but less pronounced patterns compared to those observed in mean climate space (Fig. 3).

463

464 Several metrics showed contrasting responses to climate variability. The coefficient of variation of the vertical profile (τ_{CV})
465 exhibited an inverse pattern, with highest values occurring at low climate variability (low SD in both temperature and
466 precipitation), suggesting that stable climates may promote more heterogeneous vertical canopy structures. In contrast, the
467 standard deviation of canopy height (τ_{CH}) showed the most striking pattern, exhibiting high values when temperature
468 variability exceeded 10°C and precipitation variability fell below 25 mm. Kurtosis (τ_{KU}) showed relatively modest variation
469 across climate variability space, with a weak tendency toward more negative values (more platykurtic distributions) at higher
470 precipitation variability. The standard deviation of canopy cover (τ_{CC}) showed a clear vertical gradient, with values increasing
471 primarily as a function of precipitation variability, relatively independent of temperature variability. Similarly, Shannon
472 entropy (τ_{SW}) was highest at high levels of precipitation variability combined with low to moderate temperature variability. In
473 contrast, Rao's quadratic entropy (τ_{RAO}) exhibited a bimodal pattern, reaching its highest values both at very low precipitation
474 and low temperature and, to a lesser extent, at high precipitation variability. The convex hull volume (τ_{CHV}) showed the most
475 uniform distribution across climate variability space, with generally low values and limited systematic variation. Overall,
476 metrics displayed considerably more scatter along gradients of climatic variability than in mean climate space, suggesting that
477 climate variability plays a more complex role in shaping forest structural diversity than mean climate conditions.

478

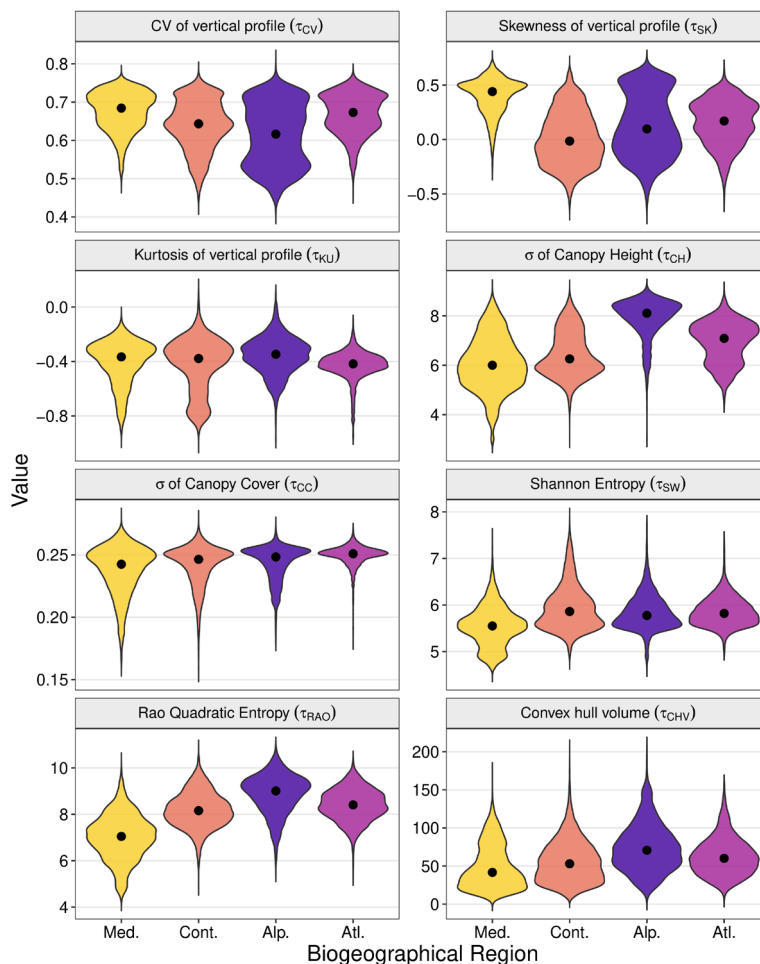
479 An examination of structural diversity patterns by biogeographic region largely reinforced the patterns revealed in the climate
480 space plots (Fig. 5, see Fig. S7 and Fig. S8 in the Supplement for the 5 km and 1 km datasets), while revealing additional
481 topographic effects. Combined horizontal-vertical diversity metrics (Shannon, Rao) were lowest in the Mediterranean region,
482 consistent with the low diversity observed in hot, arid climates, and highest in Continental, Atlantic, and Alpine regions.
483 Conversely, vertical canopy heterogeneity (Skewness τ_{SK}) was highest in the Mediterranean region, reinforcing the pattern of
484 elevated skewness at climatic extremes. Canopy height variability (τ_{CH}) was markedly elevated in the Alpine region ($M_{ed} =$
485 8.11) compared to Mediterranean ($M_{ed} = 6.00$), Continental ($M_{ed} = 6.26$), and Atlantic ($M_{ed} = 7.09$), regions likely
486 reflecting greater topographic heterogeneity. CV of vertical profile remained consistent across all regions (~0.65-0.70), while
487 (τ_{KU}) and σ of canopy cover τ_{CC} , showed minimal biogeographic variation.

488

489 A Principal Component Analysis (PCA) biplot (Fig. 6D) was used to explore the degree of intercorrelation among the eight
490 structural diversity metrics. The PCA shows that the metrics are distributed across the principal component space with
491 generally wide angular separation among vectors, indicating low to modest correlations. These patterns are consistent across
492 spatial resolutions (Fig. S9, Fig. S11D and Fig. S12D in the Supplement).

493

494



497

498

499 Figure 5. Patterns of variability in forest structural diversity metrics across European biogeographic regions. Violin plots depict the probability density
 500 distribution of eight metrics at 10 km resolution. Width represents the kernel density estimate, with black points indicating median values. Colors denote the
 501 five biogeographic regions analysed. Med. = Mediterranean region, Cont. = Continental region, Alp. = Alpine region, Atl. = Atlantic region.

502

503 3.2 Variable importance and model performance

504 The final models, derived from the stepwise backward elimination procedure, retained between 7 and 23 predictors,
 505 representing the extremes observed across various resolutions of input data and output variable types. The number of selected
 506 predictors generally increased with the resolution of the input data (Fig S10 in the Supplement). Models trained for standard
 507 deviation of canopy cover (τ_{CC}) and convex hull (τ_{CVH}) retained the highest number of predictors. In contrast, models for
 508 skewness (τ_{SK}) and Rao quadratic entropy (τ_{RAO}) retained the lowest number of predictors (Fig S10 in the Supplement).

509

510 An examination of the type of predictors selected in the final models highlighted the importance of radar-related predictors,
511 over optical ones as shown in Fig. 6A (see Fig. S11A and Fig. S12A in the Supplement for the 5 km and 1 km datasets). The
512 average proportion of radar-related variables selected across all diversity metrics and resolutions was 0.64, although there was
513 considerable variability. In general, as the resolution of the input dataset increased, the proportion of radar-related variables
514 selected through the feature elimination procedure also increased (Fig. 6A; for the 5 km and 1km datasets see Fig. S11A and
515 Fig. S12A in the Supplement). The diversity variables for which the highest number of radar-related predictors were selected
516 was the convex hull (τ_{CVH}). On the other hand, the one for which the highest number of optical-related predictors were selected,
517 was canopy cover (τ_{CC}).

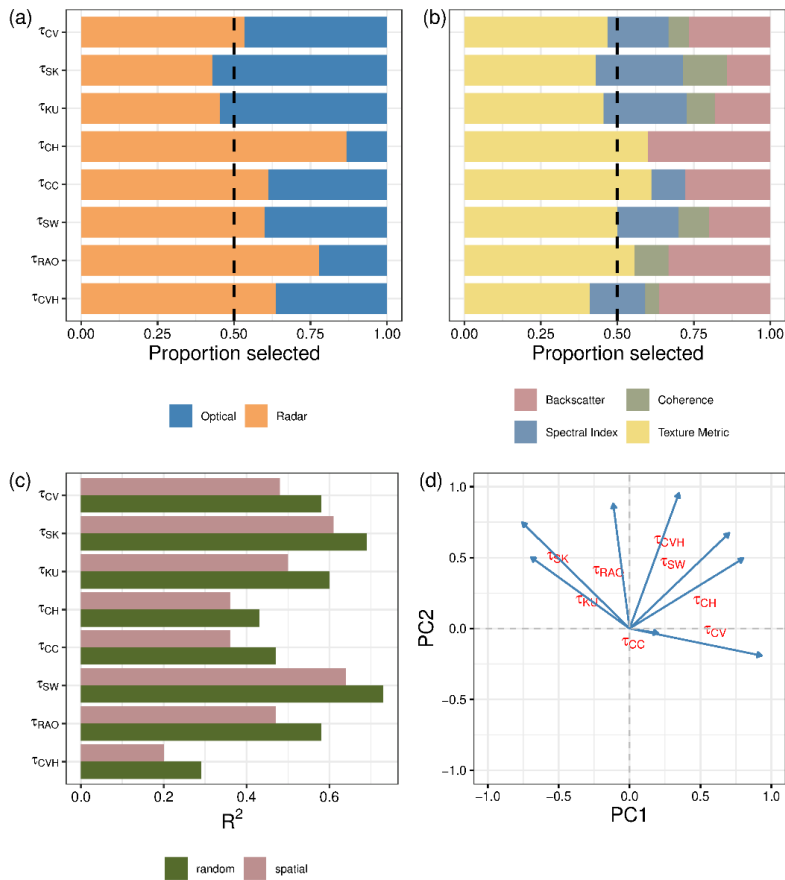
518

519 Among the predictors retained in the final models, texture-related types were the most commonly selected, followed by
520 backscatter, spectral indices, and coherence (Fig. 6B; for the 5 km and 1km datasets see Fig. S11B and Fig. S12B in the
521 Supplement). Notably, texture metrics constituted, on average, the largest proportion of selected variables at a 10 km resolution
522 (Fig 6B). Conversely, the proportion of backscatter-related variables and spectral indices increased in models using the finer
523 resolution input data (Fig. S11B and Fig. S12B in the Supplement).

524

525 Model validation revealed that random cross-validation consistently outperformed spatial cross-validation across all
526 resolutions. At 10 km resolution, the model for the Shannon the model for Shannon index τ_{SW} achieved the highest scores,
527 with 0.73 in random validation and 0.64 in spatial validation (Fig 6C and Tables B1 and B2). Conversely, the model with
528 convex hull (τ_{CVH}) as a variable showed the lowest performance, scoring 0.29 in random cross-validation and 0.20 in spatial
529 cross-validation. This difference likely reflects the contrasting statistical properties of the metrics: Shannon entropy integrates
530 information across the full distribution of GEDI observations within a spatial unit and is therefore more robust to sampling
531 variability, whereas convex hull-based metrics are more sensitive to outliers and local sampling density. The best-performing
532 models at 5 km and 1 km differed from those at 10 km, with skewness models (τ_{SK}) yielding the best results at both 5 km and
533 1 km, while canopy cover variability (τ_{CC}) was the lowest-performing at 1 km and convex hull (τ_{CVH}) at 5 km (Tables B1
534 and B2; Fig. S11C and Fig. S12C in the Supplement).

535



536

537 Figure 6. Results of the random forest modelling exercise at 10 km resolution. Panels display the variable selection frequencies (A and B)
 538 and model performance, as indicated by the R^2 values derived from two types of validation methods (C). Panel D shows the results of the
 539 Principal Component Analysis (PCA) conducted on the estimated structural diversity metrics at this resolution.

540

541 Models estimating metrics describing horizontal variability, particularly the standard deviation of canopy cover (τ_{CC}) and
 542 convex hull volume (τ_{CVH}), showed lower predictive performance, especially at finer spatial resolutions ($R^2 < 0.30$ at 1 km).
 543 These metrics rely more directly on variability among individual GEDI observations within a spatial unit, which is less
 544 consistently preserved when locally derived optical and SAR predictors are spatially aggregated to the grid-cell level. In
 545 contrast, models estimating metrics describing vertical heterogeneity and combined structural diversity (e.g. τ_{SK} , τ_{CV} , τ_{SW}),
 546 particularly at 10 km resolution, exhibited higher validation scores and greater stability across validation schemes.

547

548 An examination of the standard deviation of model outputs revealed generally increasing trend of prediction uncertainty across
 549 resolutions (Fig. S13, Fig. S14 and Fig. S15 in the Supplement), except in Rao (τ_{RAO}) and convex hull (τ_{CVH}). Overall,
 550 uncertainty was generally low across the spatial domain of interest, reflecting limited variability within the ensemble. Notable

551 exceptions occur in the Mediterranean region for the convex hull, kurtosis, and standard deviation of canopy height metrics.
552 Further variability is observed in Eastern Europe, particularly for the convex hull, skewness, kurtosis, Shannon index, and
553 standard deviation of canopy height.

554

555 **4. Discussion**

556

557 **4.1. Model-based predictions of structural diversity**

558 Our dataset provides eight metrics describing the structural heterogeneity of European forests. To our knowledge, this is the
559 first attempt to comprehensively map forest structural diversity at a quasi-continental scale (because GEDI is unable to observe
560 anything above 50° North). Datasets such as the one presented here contribute to an emerging landscape of data products based
561 on spaceborne LiDAR data, ranging from regional to global scales (e.g. Lang et al., 2023; Shendryk, 2022; Sothe et al., 2022).
562 However, while most efforts have primarily focused on mapping top canopy height, we aimed to create a set of complementary
563 metrics describing the diversity of canopy structure, an ecologically important yet neglected aspect in research.

564

565 Some of the ecological indices employed in this study are routinely applied to optical data to quantify landscape-level
566 heterogeneity using multispectral data (Tuanmu and Jetz, 2015). For instance, the Rao and Shannon diversity indices, which
567 can be calculated from spectral indices, have been widely used to quantify the heterogeneity of vegetation and are often
568 proposed as indicators of ecosystem heterogeneity (Rocchini et al., 2021). These heterogeneity indicators have proved to be
569 useful in a variety of contexts, including biodiversity modelling and quantifying the vulnerability of forest ecosystems to
570 disturbances (Forzieri et al., 2021; Taddeo et al., 2021). However, indices based solely on optical data fail to capture crucial
571 aspects of structural heterogeneity, which are related to the three-dimensional arrangement of vegetative elements in the canopy
572 (Fassnacht et al., 2022). Our study addresses a critical gap by introducing the first consistent dataset that maps structural
573 diversity across the forested domain in Europe. This development will contribute to a more detailed and robust regional analysis
574 on ecosystem dynamics, which critically depend on vegetation structure (Migliavacca et al., 2021) and structural diversity
575 (LaRue et al., 2023), and other facets of biodiversity, which requires information on the vertical profile of plants (Fassnacht et
576 al., 2022).

577

578 Our findings revealed that model performance differed according to the spatial resolutions and diversity metrics, with several
579 models achieving R^2 values indicative of moderate to strong predictive accuracy, particularly at coarser spatial resolutions
580 (Appendix B, Tables B1 and B2). This variation highlights the critical role of resolution in model performance, indicating that,
581 depending on the application of interest, coarser resolutions may optimize the utility of the models. As expected, spatial cross-
582 validation consistently yielded lower R^2 values than random train-validation random validation across most metrics and
583 resolutions. This outcome reflects the challenges inherent on machine learning methods (Meyer and Pebesma, 2021) of

584 predicting outcomes in areas geographically distinct from the training data. Nevertheless, the decrease was generally modest,
585 affirming the broad applicability of our models beyond the training domain.

586

587 The recursive feature elimination procedure highlighted the importance of textural variables (Fig. S10 in the Supplement)
588 across diversity metrics and spatial resolutions. Entropy, derived from ALOS-PALSAR-2 data, stood out as the most influential
589 variable, corroborating research that demonstrates textural metrics' effectiveness in capturing spatial heterogeneity in structural
590 diversity (Bae et al., 2019). Additionally, the significant role of coherence, which aligns with evidence of its predictive power
591 for forest structural features (Bruggisser et al., 2021; Cartus et al., 2022), suggests its potential in reflecting changes in forest
592 structural density and composition. Collectively, our findings underscore the benefits of integrating various sensor data to
593 enhance the prediction of structural diversity, as evidenced by the diverse contributions of optical and radar-based predictors.

594

595 **4.2. Potential applications**

596 We envisage that our structural diversity dataset will significantly advance future research and practical applications across
597 several disciplines. We identify three key areas where the dataset could be utilised.

598

599 Firstly, the dataset could aid in the development of different biodiversity indicators. Ecosystem structure has been identified
600 as an Essential Biodiversity Variable (EBV) (Valbuena et al., 2020), and a wide range of studies have shown a strong
601 correlation between LiDAR-based metrics and ground-based biodiversity measurements (Marselis et al., 2020). The metrics
602 developed here could be used to identify areas with unique structural features that harbour high levels of biodiversity.
603 Furthermore, integrating them with data from other sensors, such as Sentinel 1 and Sentinel 2, offers a promising avenue for
604 generating accurate spatial explicit estimates of different indicators, thus paving the way for the development of frameworks
605 for monitoring long-term biodiversity changes.

606

607 Secondly, the dataset offers a valuable resource for quantifying the observed impacts of global change drivers on the
608 functioning of European forest ecosystems. The increasing recognition of the role of structural diversity in driving ecosystem
609 processes (Ali et al., 2016; Aponte et al., 2020; Listopad et al., 2015) underscores the importance of our metrics. Consequently,
610 our dataset provides a crucial tool for enabling comprehensive, data-driven assessments of the impact of climate and land cover
611 changes on the functioning of forest ecosystems across large scales, addressing the previous limitations posed by the
612 unavailability of structural diversity data over extensive spatial scales.

613

614 Thirdly, the dataset could be used for improving Earth system models. Historically, plant canopy structure has not been
615 adequately represented in these models (Atkins et al., 2018; Schneider et al., 2020). This lack of detailed representation can
616 lead to significant errors in predicting energy balance, carbon cycling, and ecosystem responses to environmental changes
617 (Duveiller et al., 2023). Integrating structural diversity into these models has the potential to enhance the accuracy of

618 simulations by incorporating more realistic representations of light interception, photosynthetic rates, and energy fluxes. In
619 particular, these applications are directly relevant to contemporary Earth system modelling frameworks such as CMIP6 and
620 forthcoming CMIP7 simulations, which underpin IPCC climate assessments and projections.

621

622 **5. Data availability**

623 The structural diversity metrics generated in this study can be accessed at Figshare:
624 <https://doi.org/10.6084/m9.figshare.26058868> (Girardello et al., 2024). All maps are available at three spatial resolutions (1
625 km, 5 km, and 10 km) in the EPSG:3035 (LAEA) spatial reference system. All eight at all three spatial resolutions are
626 provided; users are encouraged to consult the validation results (Tables B1 and B2) to assess the suitability of individual
627 metrics for specific applications.

628 **6. Code availability**

629 Google Earth Engine code for data preparation and data for reproducing the figures are available at
630 <https://github.com/drmarcogir/structuraldiversity>

631

632 **7. Conclusions**

633

634 We generated a spatially-explicit dataset on eight forest structural diversity metrics at multiple resolutions (10km, 5km, 1km)
635 encompassing temperate, Mediterranean, and continental regions of Europe. Models developed to create the dataset were
636 robust. The dataset generated in our study represents a novel contribution to the Essential Biodiversity Variables (EBV)
637 framework, and the metrics can be used in various applications, ranging from the study of biodiversity to ecosystem
638 functioning. We conclude that combining GEDI data with those from other satellite sensors paves the way for developing a
639 consistent and scalable framework to monitor structural diversity across Europe.

640

641

642

643

644

645

646

647

648

649

650

651

652 **Appendices**

653

654 **Appendix A: Supplementary Methods**

655

656 **A1 Statistical indicators**

657 The statistical indicators used in this study are detailed below. The mean μ , standard deviation σ , skewness γ , excess kurtosis
 658 κ , coefficient of variation cv of a variable $X = \{x_1, \dots, x_N\}$ are defined as:

659

660

$$\mu(X) = \frac{1}{N} \sum_{i=1}^N x_i$$

661

$$\sigma(X) = \left\{ \frac{1}{N} \sum_{i=1}^N [x_i - \mu(X)]^2 \right\}^{1/2}$$

662

$$\gamma(X) = \frac{\sum_{i=1}^N [x_i - \mu(X)]^3}{[\sigma(X)]^3}$$

664

$$\kappa(X) = \frac{\sum_{i=1}^N [x_i - \mu(X)]^4}{[\sigma(X)]^4}$$

663

665

$$cv(X) = \frac{\sigma(X)}{\mu(X)} \quad (A1)$$

666

667 **A2 Binning in cartesian 4d space**

668

669 $p_{\varepsilon\pi o\omega}$ indicates the fraction of the GEDI shots falling in the bin identified by the indices $(\varepsilon, \pi, o, \omega)$ in the 4D cartesian space
 670 defined on the basis $(e^\varepsilon, e^\pi, e^o, e^\omega)$, see Figure S2, with

671

$$\sum_{\varepsilon\pi o\omega} p_{\varepsilon\pi o\omega} = 1 \quad (A2)$$

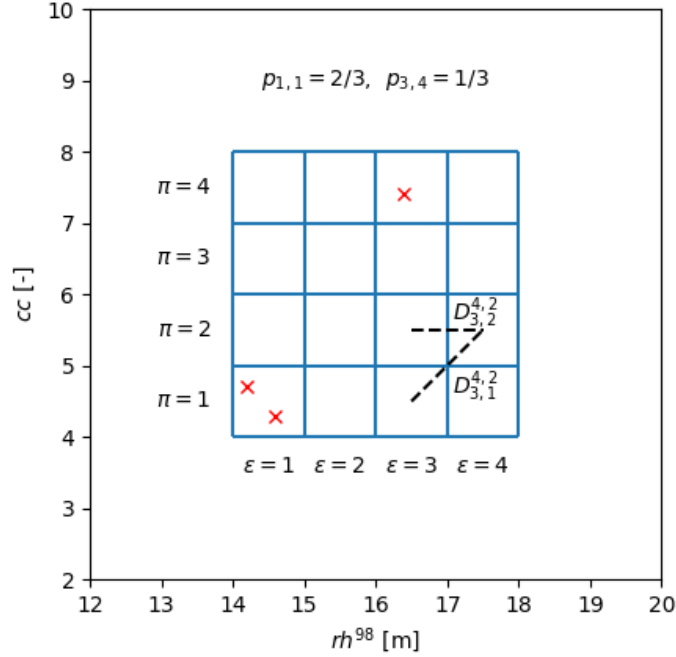
672

where $\sum_{\varepsilon\pi o\omega}$ stands for $\sum_{\varepsilon=1}^{N_{bins}^\varepsilon} \sum_{\pi=1}^{N_{bins}^\pi} \sum_{o=1}^{N_{bins}^o} \sum_{\omega=1}^{N_{bins}^\omega}$, with N_{bins}^ε number of bins in the e^ε dimension, and $D_{\varepsilon\pi o\omega}^{\varepsilon'\pi'o'\omega'}$

673

indicates the cartesian distance between $(\varepsilon, \pi, o, \omega)$ and $(\varepsilon', \pi', o', \omega')$ bin.

674



675

676 Figure A1. example of $p_{\epsilon\pi}$ and $D_{\epsilon\pi}^{\epsilon'\pi'}$ estimation in the 2D cartesian space defined on the basis (rh^{98}, cc) . The GEDI shots are
 677 reported with the red X, GEDI cc values have been amplified by 10.

678

679 A3 Predictor calculation

680 Starting with appropriate bands/indices (step 2 of the workflow in the main text), the four scalars $\phi_{\alpha,i}^{\beta}$, where $\beta \in$
 681 $\{SM, ASM, ENT, DISS\}$, are calculated from the cluster of 7×7 pixels $\phi_{\alpha,i}(p, q)$ overlapping the footprint of the GEDI shot
 682 i , where p and q represent the pixel indices within the window. In details, we calculated:

683 1. the spatial mean (SM)

$$684 \quad \phi_{\alpha,i}^{SM} = \mu(\phi_{\alpha,i}(p, q)) \quad (A3)$$

685 which is performed to compensate for potential footprint geolocation inaccuracies, and reduce the presence of noise, and three
 686 texture metrics. Texture metrics provide spatial content information (Nichol and Sarker 2011), and are highly effective in
 687 capturing the pixels heterogeneity. Defining $\bar{\phi}_{\alpha,i}(p, q)$ as the grey-levels matrix, which is calculated from $\phi_{\alpha,i}(p, q)$ by
 688 normalizing the values* within the range of $[0, 1]$ based on the 1st and 99th percentiles, $C_{\alpha,i}(m, n)$ as the corresponding grey-
 689 levels co-occurrence matrix (GLCM), with dimension 256×256 (Haralick et al. 1973):

$$690 \quad C_{\alpha,i}(m, n) = \sum_{p=1}^7 \sum_{q=1}^6 1, \text{ if } \bar{\phi}_{\alpha,i}(p, q) = m \text{ and } \bar{\phi}_{\alpha,i}(p, q+1) = n; 0, \text{ otherwise}$$

691 and $p_{\alpha,i}(m, n)$ as the probability that grey-level m occurs close to the grey-level n :

$$692 \quad p_{\alpha,i}(m, n) = \frac{c_{\alpha,i}(m,n)}{\sum_{p=0}^{255} \sum_{q=0}^{255} c_{\alpha,i}(p,q)} \quad (A4)$$

693 we calculated:

694

695 2. the angular second moment (ASM)

$$696 \quad \phi_{\alpha,i}^{ASM} = - \sum_{m=0}^{255} \sum_{n=0}^{255} [p_{\alpha,i}(m, n)]^2 \quad (A5)$$

697 ASM is a measure of the homogeneity or uniformity of pixel values within a neighbourhood. It reflects the degree to which
698 pixel values deviate from the mean, providing insights into the texture's smoothness or roughness;

699 3. the entropy

$$700 \quad \phi_{\alpha,i}^{ENT} = - \sum_{m=0}^{255} \sum_{n=0}^{255} p_{\alpha,i}(m, n) \log p_{\alpha,i}(m, n) \quad (A6)$$

701 Entropy is a measure of the randomness or disorder in the distribution of grey levels. It quantifies image non-uniformity, with
702 higher entropy values indicating a more random distribution of pixel values within a neighbourhood;

703 4. the dissimilarity index

$$704 \quad \phi_{\alpha,i}^{DISS} = \sum_{m=0}^{255} \sum_{n=0}^{255} p_{\alpha,i}(m, n) |m - n| \log p_{\alpha,i}(m, n) \quad (A7)$$

705 Dissimilarity measures the complexity and the nature of grey-level transitions among neighbouring pixels (Connors et al.
706 1984). It quantifies image contrast, with higher dissimilarity values reflecting pronounced differences among neighbouring
707 pixel values.

708 * For Sentinel-2 data, we retained only pixels with NDVI values greater than 0, as values below 0 are more likely to represent
709 non-vegetative features.

710

711

712

713

714

715

716

717

718

719

720

721

722

723 **Appendix B: Model validation results**

724

725 Table B1. Results of the random validation procedure conducted for the forest structural metrics at three spatial resolutions:
 726 1x1km, 5x5km, and 10x10km. The validation outcomes are presented in terms of the coefficient of determination (R^2), which
 727 quantifies the proportion of the variance in the dependent variable that is predictable from the independent variables.

728

Metric	1 km	5 km	10 km
CV of vertical profile (τ_{CV})	0.36	0.51	0.58
Skewness of vertical profile (τ_{SK})	0.47	0.64	0.69
Kurtosis of vertical profile (τ_{KU})	0.28	0.48	0.6
σ of Canopy Height (τ_{CH})	0.26	0.39	0.43
σ of Canopy Cover (τ_{CC})	0.16	0.37	0.47
Shannon Entropy (τ_{SW})	0.39	0.63	0.73
Rao Quadratic Entropy (τ_{RAO})	0.32	0.52	0.58
Convex Hull Volume (τ_{CHV})	0.26	0.34	0.29

729

730 Table B2. Results of the spatial cross-validation procedures conducted for the forest structural metrics at three spatial
 731 resolutions: 1x1km, 5x5km, and 10x10km. The validation outcomes are presented in terms of the coefficient of determination
 732 (R^2).

733

Metric	1 km	5 km	10 km
CV of vertical profile (τ_{CV})	0.33	0.43	0.48
Skewness of vertical profile (τ_{SK})	0.43	0.57	0.61
Kurtosis of vertical profile (τ_{KU})	0.24	0.41	0.5
σ of Canopy Height (τ_{CH})	0.25	0.34	0.36
σ of Canopy Cover (τ_{CC})	0.14	0.29	0.36
Shannon Entropy (τ_{SW})	0.36	0.55	0.64
Rao Quadratic Entropy (τ_{RAO})	0.29	0.44	0.47
Convex Hull Volume (τ_{CHV})	0.2	0.25	0.2

734

735 **Author contribution** MGir, GO and AC conceived the ideas with contributions from MM, GC, and MPicc. MGar, MPick,
736 and AE contributed to the discussion on metric development and interpretation. MGir, GO, and MPicc collated and analysed
737 the data. MGir led the writing with inputs from MPicc and GO. All authors contributed to the revision of the manuscript and
738 approved the final version.

739

740 **Competing interests** The authors declare no competing financial interests

741

742 **Acknowledgements** The study was funded by the Exploratory Project ForBioRes of the European Commission, Joint Research

743 Centre

744

745

746

747

748

749

750

751

752

753

754

755

756

757

758

759

760

761

762

763

764

765

766

767

768

769 **References**

- 770 Ali, A., Yan, E.-R., Chen, H. Y. H., Chang, S. X., Zhao, Y.-T., Yang, X.-D., and Xu, M.-S.: Stand structural diversity rather
771 than species diversity enhances aboveground carbon storage in secondary subtropical forests in Eastern China, *Biogeosciences*,
772 13, 4627–4635, <https://doi.org/10.5194/bg-13-4627-2016>, 2016.
- 773 Altmann, A., Toloşi, L., Sander, O., and Lengauer, T.: Permutation importance: a corrected feature importance measure,
774 *Bioinformatics*, 26, 1340–1347, <https://doi.org/10.1093/bioinformatics/btq134>, 2010.
- 775 Aponte, C., Kasel, S., Nitschke, C. R., Tanase, M. A., Vickers, H., Parker, L., Fedrigo, M., Kohout, M., Ruiz-Benito, P.,
776 Zavala, M. A., and Bennett, L. T.: Structural diversity underpins carbon storage in Australian temperate forests, *Global Ecology*
777 *and Biogeography*, 29, 789–802, <https://doi.org/10.1111/geb.13038>, 2020.
- 778 Aragoneses, E., García, M., Ruiz-Benito, P., and Chuvieco, E.: Mapping forest canopy fuel parameters at European scale using
779 spaceborne LiDAR and satellite data, *Remote Sens Environ*, 303, 114005, <https://doi.org/10.1016/j.rse.2024.114005>, 2024.
- 780 Atkins, J. W., Fahey, R. T., Hardiman, B. S., and Gough, C. M.: Forest Canopy Structural Complexity and Light Absorption
781 Relationships at the Subcontinental Scale, *J Geophys Res Biogeosci*, 123, 1387–1405, <https://doi.org/10.1002/2017JG004256>,
782 2018.
- 783 Bae, S., Levick, S. R., Heidrich, L., Magdon, P., Leutner, B. F., Wöllauer, S., Serebryanyk, A., Nauss, T., Krzystek, P.,
784 Gossner, M. M., Schall, P., Heibl, C., Bäessler, C., Doerfler, I., Schulze, E.-D., Krah, F.-S., Culmsee, H., Jung, K., Heurich,
785 M., Fischer, M., Seibold, S., Thorn, S., Gerlach, T., Hothorn, T., Weisser, W. W., and Müller, J.: Radar vision in the mapping
786 of forest biodiversity from space, *Nat Commun*, 10, 4757, <https://doi.org/10.1038/s41467-019-12737-x>, 2019.
- 787 Breiman, L.: Random forests, *Mach Learn*, 45, 5–32, 2001.
- 788 Bruggisser, M., Dorigo, W., Dostálová, A., Hollaus, M., Navacchi, C., Schläffer, S., and Pfeifer, N.: Potential of Sentinel-1 C-
789 Band Time Series to Derive Structural Parameters of Temperate Deciduous Forests, *Remote Sens (Basel)*, 13, 798,
790 <https://doi.org/10.3390/rs13040798>, 2021.
- 791 Cartus, O., Santoro, M., Wegmuller, U., Labriere, N., and Chave, J.: Sentinel-1 Coherence for Mapping Above-Ground
792 Biomass in Semiarid Forest Areas, *IEEE Geoscience and Remote Sensing Letters*, 19, 1–5,
793 <https://doi.org/10.1109/LGRS.2021.3071949>, 2022.
- 794 Coops, N. C., Tompalski, P., Goodbody, T. R. H., Queinnec, M., Luther, J. E., Bolton, D. K., White, J. C., Wulder, M. A., van
795 Lier, O. R., and Hermosilla, T.: Modelling lidar-derived estimates of forest attributes over space and time: A review of
796 approaches and future trends, *Remote Sens Environ*, 260, 112477, <https://doi.org/10.1016/j.rse.2021.112477>, 2021.
- 797 Coverdale, T. C. and Davies, A. B.: Unravelling the relationship between plant diversity and vegetation structural complexity:
798 A review and theoretical framework, *Journal of Ecology*, 111, 1378–1395, <https://doi.org/10.1111/1365-2745.14068>, 2023.
- 799 Crockett, E. T. H., Atkins, J. W., Guo, Q., Sun, G., Potter, K. M., Ollinger, S., Silva, C. A., Tang, H., Woodall, C. W.,
800 Holgerson, J., and Xiao, J.: Structural and species diversity explain aboveground carbon storage in forests across the United
801 States: Evidence from GEDI and forest inventory data, *Remote Sens Environ*, 295, 113703,
802 <https://doi.org/10.1016/j.rse.2023.113703>, 2023.

803 Dubayah, R., Blair, J. B., Goetz, S., Fatoyinbo, L., Hansen, M., Healey, S., Hofton, M., Hurtt, G., Kellner, J., Luthcke, S.,
804 Armston, J., Tang, H., Duncanson, L., Hancock, S., Jantz, P., Marselis, S., Patterson, P. L., Qi, W., and Silva, C.: The Global
805 Ecosystem Dynamics Investigation: High-resolution laser ranging of the Earth's forests and topography, *Science of Remote*
806 *Sensing*, 1, 100002, <https://doi.org/10.1016/j.srs.2020.100002>, 2020a.

807 Dubayah, R., Blair, J. B., Goetz, S., Fatoyinbo, L., Hansen, M., Healey, S., Hofton, M., Hurtt, G., Kellner, J., Luthcke, S., and
808 others: The Global Ecosystem Dynamics Investigation: High-resolution laser ranging of the Earth's forests and topography,
809 *Science of Remote Sensing*, 1, 100002, 2020b.

810 Duveiller, G., Pickering, M., Muñoz-Sabater, J., Caporaso, L., Boussetta, S., Balsamo, G., and Cescatti, A.: Getting the leaves
811 right matters for estimating temperature extremes, *Geosci Model Dev*, 16, 7357–7373, [https://doi.org/10.5194/gmd-16-7357-](https://doi.org/10.5194/gmd-16-7357-2023)
812 2023, 2023.

813 Ehbrecht, M., Seidel, D., Annighöfer, P., Kreft, H., Köhler, M., Zemp, D. C., Puettmann, K., Nilus, R., Babweteera, F., Willim,
814 K., Stiers, M., Soto, D., Boehmer, H. J., Fisichelli, N., Burnett, M., Juday, G., Stephens, S. L., and Ammer, C.: Global patterns
815 and climatic controls of forest structural complexity, *Nat Commun*, 12, 519, <https://doi.org/10.1038/s41467-020-20767-z>,
816 2021.

817 FAO: On definitions of forest and forest change, 2000.

818 Fassnacht, F. E., Müllerová, J., Conti, L., Malavasi, M., and Schmidlein, S.: About the link between biodiversity and spectral
819 variation, *Appl Veg Sci*, 25, <https://doi.org/10.1111/avsc.12643>, 2022.

820 Forzieri, G., Girardello, M., Ceccherini, G., Spinoni, J., Feyen, L., Hartmann, H., Beck, P. S. A., Camps-Valls, G., Chirici, G.,
821 Mauri, A., and Cescatti, A.: Emergent vulnerability to climate-driven disturbances in European forests, *Nat Commun*, 12,
822 1081, <https://doi.org/10.1038/s41467-021-21399-7>, 2021.

823 Gao, B.: NDWI—A normalized difference water index for remote sensing of vegetation liquid water from space, *Remote Sens*
824 *Environ*, 58, 257–266, [https://doi.org/10.1016/S0034-4257\(96\)00067-3](https://doi.org/10.1016/S0034-4257(96)00067-3), 1996.

825 Girardello, M., Oton, G., Piccardo, M., and Ceccherini, G.: A dataset on the structural diversity of European forests,
826 <https://doi.org/10.6084/m9.figshare.26058868.v1>, 2024.

827 Gitelson, A. and Merzlyak, M. N.: Quantitative estimation of chlorophyll-a using reflectance spectra: Experiments with autumn
828 chestnut and maple leaves, *J Photochem Photobiol B*, 22, 247–252, [https://doi.org/10.1016/1011-1344\(93\)06963-4](https://doi.org/10.1016/1011-1344(93)06963-4), 1994.

829 Gitelson, A. A. and Merzlyak, M. N.: Remote sensing of chlorophyll concentration in higher plant leaves, *Advances in Space*
830 *Research*, 22, 689–692, [https://doi.org/10.1016/S0273-1177\(97\)01133-2](https://doi.org/10.1016/S0273-1177(97)01133-2), 1998.

831 Goodbody, T. R. H., Coops, N. C., Queinnec, M., White, J. C., Tompalski, P., Hudak, A. T., Auty, D., Valbuena, R., LeBoeuf,
832 A., Sinclair, I., McCartney, G., Prieur, J.-F., and Woods, M. E.: sgsR : a structurally guided sampling toolbox for LiDAR-
833 based forest inventories, *Forestry*, 96, 411–424, <https://doi.org/10.1093/forestry/cpac055>, 2023.

834 Gorelick, N., Hancher, M., Dixon, M., Ilyushchenko, S., Thau, D., and Moore, R.: Google Earth Engine: Planetary-scale
835 geospatial analysis for everyone, *Remote Sens Environ*, 202, <https://doi.org/10.1016/j.rse.2017.06.031>, 2017.

836 Gough, C. M., Atkins, J. W., Fahey, R. T., and Hardiman, B. S.: High rates of primary production in structurally complex
837 forests, *Ecology*, 100, <https://doi.org/10.1002/ecy.2864>, 2019.

838 Hakkenberg, C. R. and Goetz, S. J.: Climate mediates the relationship between plant biodiversity and forest structure across
839 the United States, *Global Ecology and Biogeography*, 30, 2245–2258, <https://doi.org/10.1111/geb.13380>, 2021.

840 Hakkenberg, C. R., Atkins, J. W., Brodie, J. F., Burns, P., Cushman, S., Jantz, P., Kaszta, Z., Quinn, C. A., Rose, M. D., and
841 Goetz, S. J.: Inferring alpha, beta, and gamma plant diversity across biomes with GEDI spaceborne lidar, *Environmental*
842 *Research: Ecology*, 2, 035005, <https://doi.org/10.1088/2752-664X/acffed>, 2023.

843 Hancock, S., McGrath, C., Lowe, C., Davenport, I., and Woodhouse, I.: Requirements for a global lidar system: spaceborne
844 lidar with wall-to-wall coverage, *R Soc Open Sci*, 8, <https://doi.org/10.1098/rsos.211166>, 2021.

845 Hansen, M. C., Potapov, P. V., Moore, R., Hancher, M., Turubanova, S. A., Tyukavina, A., Thau, D., Stehman, S. V., Goetz,
846 S. J., Loveland, T. R., Kommareddy, A., Egorov, A., Chini, L., Justice, C. O., and Townshend, J. R. G.: High-Resolution
847 Global Maps of 21st-Century Forest Cover Change, *Science* (1979), 342, 850–853, <https://doi.org/10.1126/science.1244693>,
848 2013.

849 Holcomb, A., Burns, P., Keshav, S., and Coomes, D. A.: Repeat GEDI footprints measure the effects of tropical forest
850 disturbances, *Remote Sens Environ*, 308, 114174, <https://doi.org/10.1016/j.rse.2024.114174>, 2024.

851 Kellndorfer, J., Cartus, O., Lavallo, M., Magnard, C., Milillo, P., Oveisgharan, S., Osmanoglu, B., Rosen, P. A., and
852 Wegmüller, U.: Global seasonal Sentinel-1 interferometric coherence and backscatter data set, *Sci Data*, 9, 73,
853 <https://doi.org/10.1038/s41597-022-01189-6>, 2022.

854 Lang, N., Jetz, W., Schindler, K., and Wegner, J. D.: A high-resolution canopy height model of the Earth, *Nat Ecol Evol*, 7,
855 1778–1789, <https://doi.org/10.1038/s41559-023-02206-6>, 2023.

856 Larue, E. A., Hardiman, B. S., Elliott, J. M., and Fei, S.: Structural diversity as a predictor of ecosystem function,
857 *Environmental Research Letters*, 14, <https://doi.org/10.1088/1748-9326/ab49bb>, 2019.

858 LaRue, E. A., Hardiman, B. S., Elliott, J. M., and Fei, S.: Structural diversity as a predictor of ecosystem function,
859 *Environmental Research Letters*, 14, 114011, <https://doi.org/10.1088/1748-9326/ab49bb>, 2019.

860 LaRue, E. A., Knott, J. A., Domke, G. M., Chen, H. Y., Guo, Q., Hisano, M., Oswald, C., Oswald, S., Kong, N., Potter, K. M.,
861 and Fei, S.: Structural diversity as a reliable and novel predictor for ecosystem productivity, *Front Ecol Environ*, 21, 33–39,
862 <https://doi.org/10.1002/fee.2586>, 2023.

863 Listopad, C. M. C. S., Masters, R. E., Drake, J., Weishampel, J., and Branquinho, C.: Structural diversity indices based on
864 airborne LiDAR as ecological indicators for managing highly dynamic landscapes, *Ecol Indic*, 57, 268–279,
865 <https://doi.org/10.1016/j.ecolind.2015.04.017>, 2015.

866 Liu, C., Gong, W., Shi, S., Wang, T., Xu, T., Shi, Z., and Niu, J.: Deep learning-driven forest canopy height mapping in boreal
867 regions through multi-source remote sensing fusion: Integrating Sentinel-1/2, PALSAR, and ICESat-2/LVIS data,
868 *International Journal of Applied Earth Observation and Geoinformation*, 143, 104766,
869 <https://doi.org/10.1016/j.jag.2025.104766>, 2025.

870 Ma, Q., Su, Y., Hu, T., Jiang, L., Mi, X., Lin, L., Cao, M., Wang, X., Lin, F., Wang, B., Sun, Z., Wu, J., Ma, K., and Guo, Q.:
871 The coordinated impact of forest internal structural complexity and tree species diversity on forest productivity across forest
872 biomes, *Fundamental Research*, <https://doi.org/10.1016/j.fmre.2022.10.005>, 2022.

873 Marselis, S. M., Abernethy, K., Alonso, A., Armston, J., Baker, T. R., Bastin, J., Bogaert, J., Boyd, D. S., Boeckx, P., Burslem,
874 D. F. R. P., Chazdon, R., Clark, D. B., Coomes, D., Duncanson, L., Hancock, S., Hill, R., Hopkinson, C., Kearsley, E., Kellner,
875 J. R., Kenfack, D., Labrière, N., Lewis, S. L., Minor, D., Memiaghe, H., Monteagudo, A., Nilus, R., O'Brien, M., Phillips, O.
876 L., Poulsen, J., Tang, H., Verbeeck, H., and Dubayah, R.: Evaluating the potential of full-waveform lidar for mapping pan-
877 tropical tree species richness, *Global Ecology and Biogeography*, 29, 1799–1816, <https://doi.org/10.1111/geb.13158>, 2020.

878 Meyer, H. and Pebesma, E.: Predicting into unknown space? Estimating the area of applicability of spatial prediction models,
879 *Methods Ecol Evol*, 12, 1620–1633, <https://doi.org/10.1111/2041-210X.13650>, 2021.

880 Migliavacca, M., Musavi, T., Mahecha, M. D., Nelson, J. A., Knauer, J., Baldocchi, D. D., Perez-Priego, O., Christiansen, R.,
881 Peters, J., Anderson, K., Bahn, M., Black, T. A., Blanken, P. D., Bonal, D., Buchmann, N., Caldararu, S., Carrara, A.,
882 Carvalhais, N., Cescatti, A., Chen, J., Cleverly, J., Cremonese, E., Desai, A. R., El-Madany, T. S., Farella, M. M., Fernández-
883 Martínez, M., Filippa, G., Forkel, M., Galvagno, M., Gomasasca, U., Gough, C. M., Göckede, M., Ibrom, A., Ikawa, H.,
884 Janssens, I. A., Jung, M., Kattge, J., Keenan, T. F., Knohl, A., Kobayashi, H., Kraemer, G., Law, B. E., Liddell, M. J., Ma, X.,
885 Mammarella, I., Martini, D., Macfarlane, C., Matteucci, G., Montagnani, L., Pabon-Moreno, D. E., Panigada, C., Papale, D.,
886 Pendall, E., Penuelas, J., Phillips, R. P., Reich, P. B., Rossini, M., Rotenberg, E., Scott, R. L., Stahl, C., Weber, U., Wohlfahrt,
887 G., Wolf, S., Wright, I. J., Yakir, D., Zaehle, S., and Reichstein, M.: The three major axes of terrestrial ecosystem function,
888 *Nature*, 598, 468–472, <https://doi.org/10.1038/s41586-021-03939-9>, 2021.

889 Mueller, M. M., Dubois, C., Jagdhuber, T., Hellwig, F. M., Pathe, C., Schmullius, C., and Steele-Dunne, S.: Sentinel-1
890 Backscatter Time Series for Characterization of Evapotranspiration Dynamics over Temperate Coniferous Forests, *Remote
891 Sens (Basel)*, 14, 6384, <https://doi.org/10.3390/rs14246384>, 2022.

892 Murphy, B. A., May, J. A., Butterworth, B. J., Andresen, C. G., and Desai, A. R.: Unraveling Forest Complexity: Resource
893 Use Efficiency, Disturbance, and the Structure-Function Relationship, *J Geophys Res Biogeosci*, 127,
894 <https://doi.org/10.1029/2021JG006748>, 2022.

895 Naidoo, L., Mathieu, R., Main, R., Kleynhans, W., Wessels, K., Asner, G., and Leblon, B.: Savannah woody structure
896 modelling and mapping using multi-frequency (X-, C- and L-band) Synthetic Aperture Radar data, *ISPRS Journal of
897 Photogrammetry and Remote Sensing*, 105, 234–250, <https://doi.org/10.1016/j.isprsjprs.2015.04.007>, 2015.

898 Pan, J., Zhao, R., Xu, Z., Cai, Z., and Yuan, Y.: Quantitative estimation of sentinel-1A interferometric decorrelation using
899 vegetation index, *Front Earth Sci (Lausanne)*, 10, <https://doi.org/10.3389/feart.2022.1016491>, 2022.

900 Perrone, M., Conti, L., Galland, T., Komárek, J., Lagner, O., Torresani, M., Rossi, C., Carmona, C. P., de Bello, F., Rocchini,
901 D., Moudrý, V., Šímová, P., Bagella, S., and Malavasi, M.: “Flower power”: How flowering affects spectral diversity metrics
902 and their relationship with plant diversity, *Ecol Inform*, 81, 102589, <https://doi.org/10.1016/j.ecoinf.2024.102589>, 2024.

903 Potapov, P., Li, X., Hernandez-Serna, A., Tyukavina, A., Hansen, M. C., Kommareddy, A., Pickens, A., Turubanova, S., Tang,
904 H., Silva, C. E., Armston, J., Dubayah, R., Blair, J. B., and Hofton, M.: Mapping global forest canopy height through
905 integration of GEDI and Landsat data, *Remote Sens Environ*, 253, 112165, <https://doi.org/10.1016/j.rse.2020.112165>, 2021.

906 Qi, J., Chehbouni, A., Huete, A. R., Kerr, Y. H., and Sorooshian, S.: A modified soil adjusted vegetation index, *Remote Sens*
907 *Environ*, 48, 119–126, [https://doi.org/10.1016/0034-4257\(94\)90134-1](https://doi.org/10.1016/0034-4257(94)90134-1), 1994.

908 Roberts, D. R., Bahn, V., Ciuti, S., Boyce, M. S., Elith, J., Guillera-Arroita, G., Hauenstein, S., Lahoz-Monfort, J. J., Schröder,
909 B., Thuiller, W., Warton, D. I., Wintle, B. A., Hartig, F., and Dormann, C. F.: Cross-validation strategies for data with temporal,
910 spatial, hierarchical, or phylogenetic structure, *Ecography*, n/a--n/a, <https://doi.org/10.1111/ecog.02881>, 2016.

911 Rocchini, D., Thouverai, E., Marcantonio, M., Iannacito, M., Da Re, D., Torresani, M., Bacaro, G., Bazzichetto, M., Bernardi,
912 A., Foody, G. M., Furrer, R., Kleijn, D., Larsen, S., Lenoir, J., Malavasi, M., Marchetto, E., Messori, F., Montagni, A., Moudrý,
913 V., Naimi, B., Ricotta, C., Rossini, M., Santi, F., Santos, M. J., Schaeppman, M. E., Schneider, F. D., Schuh, L., Silvestri, S.,
914 Šímová, P., Skidmore, A. K., Tattoni, C., Tordoni, E., Vicario, S., Zannini, P., and Wegmann, M.: rasterdiv—An Information
915 Theory tailored R package for measuring ecosystem heterogeneity from space: To the origin and back, *Methods Ecol Evol*,
916 12, 1093–1102, <https://doi.org/10.1111/2041-210X.13583>, 2021.

917 Rouse, J. W., Haas, R. H., Schell, J. A., Deering, D. W., and others: Monitoring vegetation systems in the Great Plains with
918 ERTS, *NASA Spec. Publ*, 351, 309, 1974.

919 Schneider, F. D., Ferraz, A., Hancock, S., Duncanson, L. I., Dubayah, R. O., Pavlick, R. P., and Schimel, D. S.: Towards
920 mapping the diversity of canopy structure from space with GEDI, *Environmental Research Letters*, 15,
921 <https://doi.org/10.1088/1748-9326/ab9e99>, 2020.

922 Schwartz, M., Ciais, P., Ottlé, C., De Truchis, A., Vega, C., Fayad, I., Brandt, M., Fensholt, R., Baghdadi, N., Morneau, F.,
923 Morin, D., Guyon, D., Dayau, S., and Wigneron, J.-P.: High-resolution canopy height map in the Landes forest (France) based
924 on GEDI, Sentinel-1, and Sentinel-2 data with a deep learning approach, *International Journal of Applied Earth Observation*
925 *and Geoinformation*, 128, 103711, <https://doi.org/10.1016/j.jag.2024.103711>, 2024.

926 Shendryk, Y.: Fusing GEDI with earth observation data for large area aboveground biomass mapping, *International Journal of*
927 *Applied Earth Observation and Geoinformation*, 115, 103108, <https://doi.org/10.1016/j.jag.2022.103108>, 2022.

928 Shimada, M., Itoh, T., Motooka, T., Watanabe, M., Shiraishi, T., Thapa, R., and Lucas, R.: New global forest/non-forest maps
929 from ALOS PALSAR data (2007–2010), *Remote Sens Environ*, 155, 13–31, <https://doi.org/10.1016/j.rse.2014.04.014>, 2014.

930 Shugart, H. H., Saatchi, S., and Hall, F. G.: Importance of structure and its measurement in quantifying function of forest
931 ecosystems, *J Geophys Res Biogeosci*, 115, <https://doi.org/10.1029/2009JG000993>, 2010.

932 Sothe, C., Gonsamo, A., Lourenço, R. B., Kurz, W. A., and Snider, J.: Spatially Continuous Mapping of Forest Canopy Height
933 in Canada by Combining GEDI and ICESat-2 with PALSAR and Sentinel, *Remote Sens (Basel)*, 14, 5158,
934 <https://doi.org/10.3390/rs14205158>, 2022.

935 Sun, J., Yu, X., Wang, H., Jia, G., Zhao, Y., Tu, Z., Deng, W., Jia, J., and Chen, J.: Effects of forest structure on hydrological
936 processes in China, *J Hydrol (Amst)*, 561, 187–199, <https://doi.org/10.1016/j.jhydrol.2018.04.003>, 2018.

937 Taddeo, S., Dronova, I., and Harris, K.: Greenness, texture, and spatial relationships predict floristic diversity across wetlands
938 of the conterminous United States, *ISPRS Journal of Photogrammetry and Remote Sensing*, 175, 236–246,
939 <https://doi.org/10.1016/j.isprsjprs.2021.03.012>, 2021.

940 Toda, M., Knohl, A., Luysaert, S., and Hara, T.: Simulated effects of canopy structural complexity on forest productivity, *For*
941 *Ecol Manage*, 538, 120978, <https://doi.org/10.1016/j.foreco.2023.120978>, 2023.

942 Tuanmu, M. and Jetz, W.: A global, remote sensing-based characterization of terrestrial habitat heterogeneity for biodiversity
943 and ecosystem modelling, *Global Ecology and Biogeography*, 24, 1329–1339, <https://doi.org/10.1111/geb.12365>, 2015.

944 Valbuena, R., O’Connor, B., Zellweger, F., Simonson, W., Vihervaara, P., Maltamo, M., Silva, C. A., Almeida, D. R. A.,
945 Danks, F., Morsdorf, F., Chirici, G., Lucas, R., Coomes, D. A., and Coops, N. C.: Standardizing Ecosystem Morphological
946 Traits from 3D Information Sources, *Trends Ecol Evol*, 35, 656–667, <https://doi.org/10.1016/j.tree.2020.03.006>, 2020.

947 Vollrath, A., Mullissa, A., and Reiche, J.: Angular-Based Radiometric Slope Correction for Sentinel-1 on Google Earth Engine,
948 *Remote Sens (Basel)*, 12, 1867, <https://doi.org/10.3390/rs12111867>, 2020.

949 Wang, C., Zhang, W., Ji, Y., Marino, A., Li, C., Wang, L., Zhao, H., and Wang, M.: Estimation of Aboveground Biomass for
950 Different Forest Types Using Data from Sentinel-1, Sentinel-2, ALOS PALSAR-2, and GEDI, *Forests*, 15, 215,
951 <https://doi.org/10.3390/f15010215>, 2024.

952 Zhai, L., Will, R. E., and Zhang, B.: Structural diversity is better associated with
953 forest productivity than species or functional diversity, *Ecology*, 105, <https://doi.org/10.1002/ecy.4269>, 2024.